

Prospects for Hypercharged Anomaly Mediated SUSY Breaking at the LHC

Howard Baer^{1*}, Radovan Dermíšek^{2†}, Shibi Rajagopalan^{1‡}, Heaya Summy^{1§}

1. *Dept. of Physics and Astronomy, University of Oklahoma, Norman, OK 73019, USA*
2. *Dept. of Physics, Indiana University, Bloomington IN 47405, USA*

Abstract

We investigate the phenomenological consequences of string models wherein the MSSM resides on a D-brane, and the hypercharge gaugino mass is generated in a geometrically separated hidden sector. This hypercharged anomaly-mediated SUSY breaking (HCAMSB) model naturally solves the tachyonic slepton mass problem endemic to pure AMSB scenarios. In HCAMSB, one obtains a mass ordering $M_1 > \mu > M_2$ with split left- and right-scalars, whereas in mAMSB models, one obtains $\mu > M_1 > M_2$ with nearly degenerate left- and right- scalars. We compute the allowed parameter space and expected superparticle mass spectrum in the HCAMSB model. For low values of the HC and AMSB mixing parameter α , the spectra is characterized by light left-sleptons, while the spectra for large α is characterized by light top- and bottom- squarks. We map out the approximate reach of LHC for HCAMSB, and find that with 100 fb^{-1} of integrated luminosity, a gravitino mass of ~ 115 (105) TeV can be probed for low (high) values of α , corresponding to a gluino mass reach of ~ 2.4 (2.2) TeV. Both cases contain— as is typical in AMSB models— long lived charginos that should yield visible highly ionizing tracks in the LHC detector. Also, in the lower $\tan \beta$ range, HCAMSB models give rise to reconstructable $Z \rightarrow \ell\bar{\ell}$ candidates in SUSY cascade decay events, while mAMSB models should do so only rarely.

*Email: baer@nhn.ou.edu

†Email: dermisek@indiana.edu

‡Email: shibi@nhn.ou.edu

§Email: heaya@nhn.ou.edu

1 Introduction

Anomaly-mediated supersymmetry breaking (AMSB) models have received much attention in the literature due to their attractive properties[1]: the soft supersymmetry (SUSY) breaking terms are completely calculable in terms of just one free parameter (the gravitino mass, $m_{3/2}$), the soft terms are real and flavor invariant, thus solving the SUSY flavor and CP problems, the soft terms are actually renormalization group invariant[2], and can be calculated at any convenient scale choice. In order to realize the AMSB set-up, the hidden sector must be “sequestered” on a separate brane from the observable sector in an extra-dimensional universe, so that tree-level supergravity breaking terms do not dominate the soft term contributions. Such a set-up can be realized in brane-worlds, where SUSY breaking takes place on one brane, with the visible sector residing on a separate brane. The soft SUSY breaking (SSB) terms arise from the rescaling anomaly.

In spite of its attractive features, AMSB models suffer from the well-known problem that slepton mass-squared parameters are found to be negative, giving rise to tachyonic states. The original solution to this problem is to suppose that scalars acquire as well a universal mass m_0 , which when added to the AMSB SSB terms, renders them positive. Thus, the parameter space of the “minimal” AMSB model (mAMSB) is given by

$$m_0, m_{3/2}, \tan \beta, \text{sign}(\mu). \quad (1)$$

An alternative set-up for AMSB has been advocated in Ref. [3], known as hypercharged anomaly-mediation (HCAMSB). It is a string motivated scenario which uses a similar setup as the one envisioned for AMSB. In HCAMSB, SUSY breaking is localized at the bottom of a strongly warped hidden region, geometrically separated from the visible region where the MSSM resides. The warping suppresses contributions due to tree-level gravity mediation[4] and the anomaly mediation[1] can become the dominant source of SUSY breaking in the visible sector. Possible exceptions to this sequestering mechanism are gaugino masses of $U(1)$ gauge symmetries [5]. Thus, in the MSSM, the mass of the bino– the gaugino of $U(1)_{Y-}$ – can be the only soft SUSY breaking parameter not determined by anomaly mediation[3]. Depending on its size, the bino mass M_1 can lead to a small perturbation to the spectrum of anomaly mediation, or it can be the largest soft SUSY breaking parameter in the visible sector: as a result of RG evolution its effect on other soft SUSY breaking parameters can dominate the contribution from anomaly mediation. In extensions of the MSSM, additional $U(1)$ ’s can also communicate SUSY breaking to the MSSM sector [6].

Besides sharing the same theoretical setup, anomaly mediation and hypercharge mediation cure phenomenological shortcomings of each other. The minimal AMSB model predicts a negative mass squared for the sleptons (and features relatively heavy squarks). On the other hand, the pure hypercharge mediation suffers from negative squared masses for stops and sbottoms (and features relatively heavy sleptons): see Sec. 2. As a result, the combination of hypercharge and anomaly mediation leads to phenomenologically viable spectra for a sizable range of relative contributions [3].

We parametrize the HCAMSB SSB contribution \tilde{M}_1 using a dimensionless quantity α such that $\tilde{M}_1 = \alpha m_{3/2}$ so that α governs the size of the hypercharge contribution to soft terms

relative to the AMSB contribution. Then the parameter space of HCAMSB models is given by

$$\alpha, m_{3/2}, \tan\beta, \text{sign}(\mu). \quad (2)$$

In the HCAMSB model, we assume as usual that electroweak symmetry is broken radiatively by the large top-quark Yukawa coupling. Then the SSB B term and the superpotential μ term are given as usual by the scalar potential minimization conditions which emerge from requiring an appropriate breakdown of electroweak symmetry.

In HCAMSB, we take the SSB terms to be of the form:

$$\begin{aligned} M_1 &= \tilde{M}_1 + \frac{b_1 g_1^2}{16\pi^2} m_{3/2}, \\ M_a &= \frac{b_a g_a^2}{16\pi^2} m_{3/2}, \quad a = 2, 3 \\ m_i^2 &= -\frac{1}{4} \left\{ \frac{d\gamma}{dg} \beta_g + \frac{d\gamma}{df} \beta_f \right\} m_{3/2}^2 \\ A_f &= \frac{\beta_f}{f} m_{3/2}, \end{aligned} \quad (3)$$

where $(b_1, b_2, b_3) = (33/5, 1, -3)$, β_f is the beta function for the corresponding superpotential coupling, and $\gamma = \partial \ln Z / \partial \ln \mu$ with Z the wave function renormalization constant. The wino and gluino masses (M_2 and M_3) receive a contribution from the bino mass at the two loop level. Thus, in pure hypercharge mediation, they are one loop suppressed compared to the scalar masses. For convenience, we assume the above SSB mass parameters are input at the GUT scale, and all weak scale SSB parameters are determined by renormalization group evolution.

We have included the above HCAMSB model into the Isasugra subprogram of the event generator Isajet v7.79[7]. After input of the above parameter set, Isasugra then implements an iterative procedure of solving the MSSM RGEs for the 26 coupled renormalization group equations, taking the weak scale measured gauge couplings and third generation Yukawa couplings as inputs, as well as the above-listed GUT scale SSB terms. Isasugra implements full 2-loop RG running in the \overline{DR} scheme, and minimizes the RG-improved 1-loop effective potential at an optimized scale choice $Q = \sqrt{m_{\tilde{t}_L} m_{\tilde{t}_R}}$ [8] to determine the magnitude of μ and m_A . All physical sparticle masses are computed with complete 1-loop corrections, and 1-loop weak scale threshold corrections are implemented for the t , b and τ Yukawa couplings[9]. The off-set of the weak scale boundary conditions due to threshold corrections (which depend on the entire superparticle mass spectrum), necessitates an iterative up-down RG running solution. The resulting superparticle mass spectrum is typically in close accord with other sparticle spectrum generators[10].

Once the weak scale sparticle mass spectrum is known, then sparticle production cross sections and branching fractions may be computed, and collider events may be generated. Then, signatures for HCAMSB at the CERN LHC may be computed and compared against Standard Model (SM) backgrounds. Our goal in this paper is to characterize the HCAMSB parameter space and sparticle mass spectrum, and derive consequences for the CERN LHC pp collider, which is expected to begin operation in Fall, 2009. Some previous investigations of mAMSB at LHC have been reported in Ref. [11, 12, 13].

The remainder of this paper is organized as follows. In Sec. 2, we calculate the allowed parameter space of HCAMSB models, imposing various experimental and theoretical constraints. We also show sample mass spectra from HCAMSB models, and show their variation with α and $m_{3/2}$. We show typical values of $BF(b \rightarrow s\gamma)$ and $(g-2)_\mu$ that result. In Sec. 3, we explore consequences of the HCAMSB model for LHC sparticle searches. Typically, collider events are characterized by production of high p_T b and t quarks, along with E_T^{miss} and observable tracks from late decaying charginos \widetilde{W}_1^\pm . For small α , slepton pair production may be visible, while for large α , direct $\tilde{t}_1\tilde{t}_1$ and $\tilde{b}_1\tilde{b}_1$ production may be visible. The LHC reach for 100 fb $^{-1}$ should extend up to $m_{3/2} \sim 115$ (105) TeV, corresponding to a reach in $m_{\tilde{g}} \sim 2.4$ (2.2) TeV, for small (large) values of α . The HCAMSB model should be easily distinguishable from the mAMSB model at the LHC if $\tan\beta$ is not too large, due to the presence of $Z \rightarrow \ell\bar{\ell}$ candidates in cascade decay events. The presence of these reflects the mass ordering $M_1 > \mu > M_2$ in the HCAMSB model, while $\mu > M_1 > M_2$ in the mAMSB model. In Sec. 4, we present our conclusions and outlook for HCAMSB models.

2 Mass spectra, parameter space and constraints on the HCAMSB model

2.1 Spectra and parameter space

We begin our discussion by plotting out in Fig. 1 the mass spectra of various sparticles versus $a)$ $m_0/m_{3/2}$ in mAMSB and $b)$ α in the HCAMSB model, for $m_{3/2}$ fixed at 50 TeV, while taking $\tan\beta = 10$, $\mu > 0$ and $m_t = 172.6$ GeV. For m_0 and $\alpha \sim 0$, the yellow-shaded region yields the well-known tachyonic slepton mass-squared values, which could lead to electric charge non-conservation in the scalar potential. In mAMSB, as m_0 increases, all the scalars increase in mass, while $m_{\tilde{g}}$, $m_{\tilde{W}_1}$ and $m_{\tilde{Z}_1}$ remain roughly constant, and the superpotential μ term decreases. The large m_0 limit of parameter space is reached around $m_0/m_{3/2} \sim 0.075$, where EWSB is no longer properly broken (signaled by $\mu^2 < 0$). We also see the well-known property of mAMSB models that $m_{\tilde{e}_L} \simeq m_{\tilde{e}_R}$. In addition, an important distinction between the two models is the mass ordering which enters into the neutralino mass matrix: we find typically that $M_1 > \mu > M_2$ in the HCAMSB model, while $\mu > M_1 > M_2$ in mAMSB. Thus, both models will have a wino-like \tilde{Z}_1 state. However, in the HCAMSB model, the $\tilde{Z}_{2,3}$ are dominantly higgsino-like states, with \tilde{Z}_4 being bino-like, while in the mAMSB model, we expect \tilde{Z}_2 to be bino-like with $\tilde{Z}_{3,4}$ being higgsino-like. This mass ordering difference will give rise to a crucial distinction in LHC SUSY cascade decay events (see Sec. 3) which may serve to distinguish the two models.

In the HCAMSB case, as α increases, the GUT scale gaugino mass M_1 increases. Thus, the bino mass increases with α , while the light charginos \widetilde{W}_1^\pm and neutralino \tilde{Z}_1 remain wino-like with mass fixed near M_2 , and the gluino remains with mass fixed at nearly $M_3 \sim 0.022m_{3/2}$. Many of the scalar masses also vary with α . The reason is that as α increases, so does the GUT scale value of M_1 . The large value of M_1 feeds into the scalar masses via their renormalization group equations, causing many of them to increase with α , with the largest increases occurring for the scalars with the largest weak hypercharge assignments Y . Thus, we see strong increases

in the \tilde{u}_R , \tilde{e}_L and especially the \tilde{e}_R masses with increasing $|\alpha|$. The \tilde{u}_L squark only receives a small increase in mass, since its hypercharge value is quite small: $Y = 1/3$. From Fig. 1b), we already see an important distinction between mAMSB and HCAMSB models: in the former case, the \tilde{e}_L and \tilde{e}_R states are nearly mass degenerate, while in the latter case these states are highly split, with $m_{\tilde{e}_R} \gg m_{\tilde{e}_L}$.

An exception to the mass increase with α in Fig. 1b) occurs in the values of $m_{\tilde{t}_1}$ and $m_{\tilde{b}_1}$. In these cases, the large increase in $m_{\tilde{U}_3}^2$ feeds into the RGE $X_t = m_{\tilde{Q}_3}^2 + m_{\tilde{U}_3}^2 + m_{H_u}^2 + A_t^2$ term[14], and *amplifies* the top-quark Yukawa coupling suppression of the $m_{\tilde{Q}_3}^2$ term. Since the doublet \tilde{Q}_3 contains both the \tilde{t}_L and \tilde{b}_L states, both of these actually suffer a *decrease* in mass with increasing α . Thus, we expect in HCAMSB models with moderate to large α that the third generation squark states will be highly split. For large $|\alpha|$, we expect the light third generation squarks \tilde{t}_1 and \tilde{b}_1 to be quite light, with a dominantly left- squark composition. The heavier squarks \tilde{t}_2 and \tilde{b}_2 will be quite heavy, and dominantly right-squark states.

In addition, we see from Fig. 1b) that the superpotential μ term *decreases* with increasing α . At moderate-to-large $\tan\beta$, the μ term is— from the tree-level scalar potential minimization conditions— $\mu^2 \simeq -m_{H_u}^2$. The running of $m_{H_u}^2$ versus energy scale Q is shown in Fig. 2 for $\alpha = 0.025, 0.1$ and 0.195 . We see that as α increases, the value of $-m_{H_u}^2$ actually decreases, leading to a small μ^2 value. The relevant RGE reads

$$\frac{dm_{H_u}^2}{dt} = \frac{2}{16\pi^2} \left(-\frac{3}{5}g_1^2M_1^2 - 3g_2^2M_2^2 + \frac{3}{10}g_1^2S + 3f_t^2X_t \right). \quad (4)$$

A large value of M_1 thus leads to an *upwards* push to $m_{H_u}^2$ in its early running from $Q = M_{GUT}$, which is only later compensated by the downward push of the Yukawa-coupling term involving the top Yukawa coupling f_t . In the figure, for the case of $\alpha = 0.195$, the weak scale value of $m_{H_u}^2$ is actually positive. Upon adding the large 1-loop corrections to the effective potential (due to the light top-squark), the RG-improved scalar potential yields a positive value of μ^2 . Thus, in the region of large α , where μ becomes small and comparable to M_2 , we expect the neutralino \tilde{Z}_1 to become a mixed wino-higgsino particle, and the corresponding $\Delta m = m_{\tilde{W}_1} - m_{\tilde{Z}_1}$ mass gap to increase beyond the value $\Delta m \sim 150$ MeV which is expected in AMSB models[15].

An interesting coincidence related to the RG evolution of $m_{H_u}^2$ in the limit where hypercharge mediation dominates is that the electroweak symmetry breaking *requires* the electroweak scale to be $\sim (12 - 16)$ orders of magnitude below the scale M_\star (M_\star may be of order the GUT scale or string scale) at which the Bino mass M_1 is generated. If the hierarchy between the electroweak scale and M_\star was smaller, then a SUSY breaking scenario in which hypercharge mediation dominates would not be capable of triggering EWSB (the energy interval for RG evolution would not be large enough to drive the $m_{H_u}^2$ parameter to negative values). This is a very uncommon feature among SUSY breaking scenarios.¹

For a more detailed comparison, we list in Table 1 the sparticle mass spectrum for a mAMSB point with $m_0 = 300$ GeV, $m_{3/2} = 50$ TeV, $\tan\beta = 10$ and $\mu > 0$, and two HCAMSB points with small and large α values equal to 0.025 and 0.195. While all three cases have a comparable gluino mass, we see that the rather small splitting amongst $\tilde{u}_L - \tilde{u}_R$ and also $\tilde{e}_L - \tilde{e}_R$ states

¹A similar feature can be found in scenarios with negative stop masses squared at the unification scale [16]. For more details, see also Ref. [17].

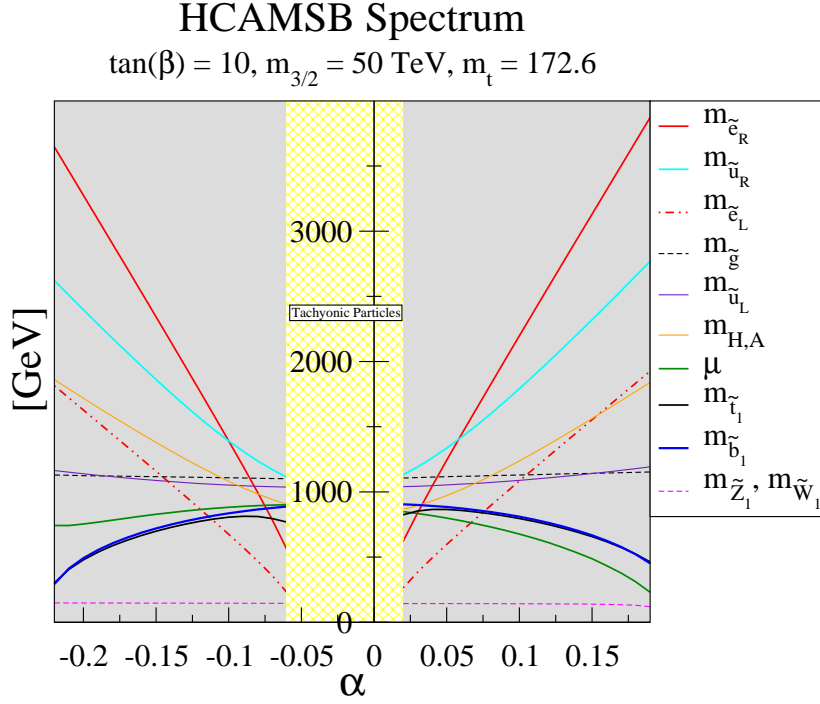
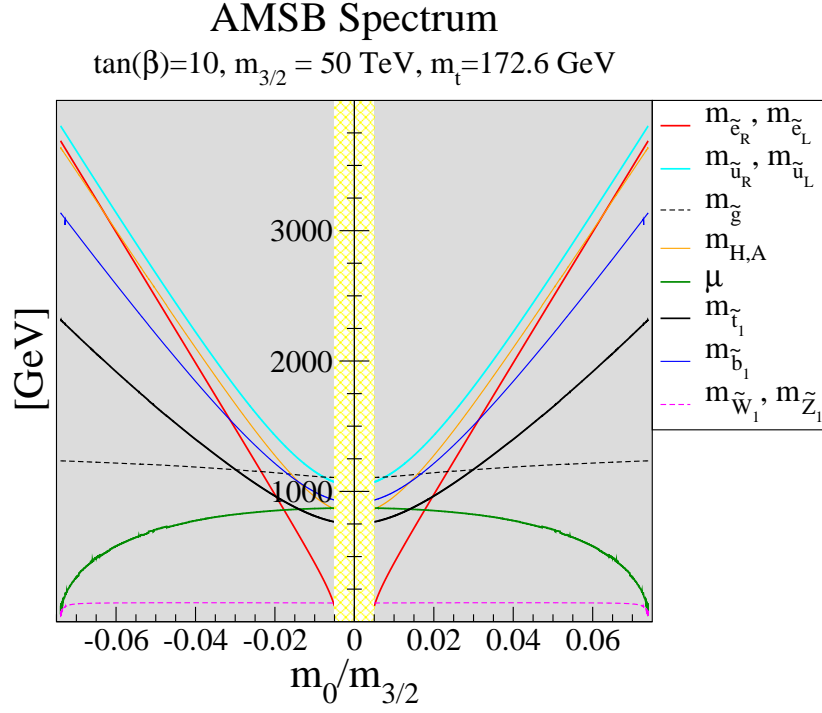


Figure 1: Sparticle mass spectrum versus a). $m_0/m_{3/2}$ in mAMSB and b). α in the HCAMSB model, for $m_{3/2} = 50 \text{ TeV}$ and $\tan \beta = 10$, with $\mu > 0$ and $m_t = 172.6 \text{ GeV}$.

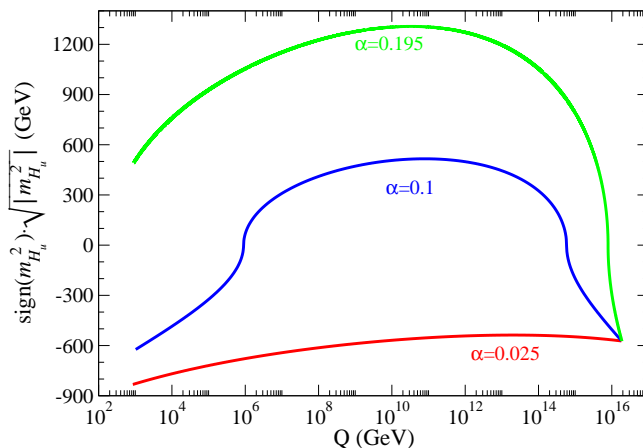


Figure 2: Running of the $m_{H_u}^2$ parameter as a function of energy scale Q for $\alpha = 0.025, 0.1$ and 0.195 for $m_{3/2} = 50$ TeV and $\tan\beta = 10$, $\mu > 0$ in the HCAMSB model.

in mAMSB is turned to large left-right splitting in the HCAMSB cases. We also see that the $m_{\tilde{W}_1} - m_{\tilde{Z}_1} \sim 150$ MeV mass gap in AMSB and HCAMSB1– which leads to long-lived and possibly observable \tilde{W}_1 tracks in collider detectors– opens up to a few GeV in the HCAMSB2 case. The latter mass gap is large enough to make the \tilde{W}_1 state less long lived, although still maintaining possibly measureable tracks in collider scattering events. The value of $c\tau_{\tilde{W}_1}$ versus α is shown in Fig. 3, where we usually get $c\tau_{\tilde{W}_1} \sim 10 - 100$ mm for most α values. The value drops to shorter lengths for large α . The shorter travel time of the \tilde{W}_1 would distinguish the large α HCAMSB case with a mixed higgsino-wino \tilde{Z}_1 state from the low α HCAMSB case where \tilde{Z}_1 is instead nearly pure wino-like.

We show in Fig. 4 a cartoon of the mass spectra for mAMSB and HCAMSB taken at the same values of $m_{3/2} = 50$ TeV, $\tan\beta = 10$ and $\mu > 0$. For mAMSB, we take $m_0 = 300$ GeV, while for HCAMSB, we take $\alpha = 0.1$. The figure illustrates quickly the main features of a left-right scalar degeneracy in mAMSB, but a left-right split spectrum of HCAMSB models. It also illustrates the $\mu > M_1 > M_2$ ordering in mAMSB, and $M_1 > \mu > M_2$ in HCAMSB via the location of the wino, higgsino and bino states.

Next, we display the allowed parameter space of the HCAMSB model in the $m_{3/2}$ vs. α plane in Fig. 5 for *a*). $\tan\beta = 10$ and *b*). $\tan\beta = 40$, where we also take $\mu > 0$ and $m_t = 172.6$ GeV. The yellow shaded region around $\alpha \sim 0$ is dis-allowed because this region generates tachyonic slepton masses. The large $|\alpha|$ solutions are forbidden due to a lack of appropriate breakdown of electroweak symmetry (here signaled by a superpotential term $\mu^2 < 0$). Over most of parameter space, the lightest SUSY particle is the wino-like neutralino \tilde{Z}_1 , although for large $|\alpha|$, the \tilde{Z}_1 becomes a mixed higgsino-wino state (due to $|\mu|$ becoming small, and comparable to the $SU(2)$ gaugino mass M_2). In the case of nearly degenerate and wino-like \tilde{Z}_1 and \tilde{W}_1 states– as occurs in generic AMSB models– the mass limit on the light chargino extracted by searches at LEP2 is that $m_{\tilde{W}_1} > 91.9$ GeV[18]. Solutions with $m_{\tilde{W}_1}$ less than this limit occur in the shaded region of the plot at low $m_{3/2}$, and so this region yields the low $m_{3/2}$

parameter	mAMSB	HCAMSB1	HCAMSB2
α	—	0.025	0.195
m_0	300	—	—
$m_{3/2}$	50 TeV	50 TeV	50 TeV
$\tan \beta$	10	10	10
M_1	460.3	997.7	4710.5
M_2	140.0	139.5	137.5
μ	872.8	841.8	178.8
$m_{\tilde{g}}$	1109.2	1107.6	1154.2
$m_{\tilde{u}_L}$	1078.2	1041.3	1199.1
$m_{\tilde{u}_R}$	1086.2	1160.3	2826.3
$m_{\tilde{t}_1}$	774.9	840.9	427.7
$m_{\tilde{t}_2}$	985.3	983.3	2332.5
$m_{\tilde{b}_1}$	944.4	902.6	409.0
$m_{\tilde{b}_2}$	1076.7	1065.7	1650.7
$m_{\tilde{e}_L}$	226.9	326.3	1973.1
$m_{\tilde{e}_R}$	204.6	732.3	3964.9
$m_{\tilde{W}_2}$	879.2	849.4	233.1
$m_{\tilde{W}_1}$	143.9	143.5	107.1
$m_{\tilde{Z}_4}$	878.7	993.7	4727.2
$m_{\tilde{Z}_3}$	875.3	845.5	228.7
$m_{\tilde{Z}_2}$	451.1	839.2	188.6
$m_{\tilde{Z}_1}$	143.7	143.3	105.0
m_A	878.1	879.6	1875.1
m_h	113.8	113.4	112.1
$\Omega_{\tilde{Z}_1} h^2$	0.0016	0.0015	0.0011
$BF(\tilde{Z}_2 \rightarrow \tilde{Z}_1 Z)$	0.01%	7.7%	22.3%
σ [fb]	7.7×10^3	7.4×10^3	1.8×10^4
\tilde{g}, \tilde{q} pairs	15.0%	15.5%	14.3%
<i>EW – ino pairs</i>	79.7%	81.9%	85%
<i>slep. pairs</i>	3.7%	0.8%	—
$\tilde{t}_1 \tilde{t}_1$	0.4%	0.2%	5.5%

Table 1: Masses and parameters in GeV units for three case study points AMSB, HCAMSB1 and HCAMSB2 using Isajet 7.79 with $m_t = 172.6$ GeV and $\mu > 0$. We also list the total tree level sparticle production cross section in fb at the LHC.

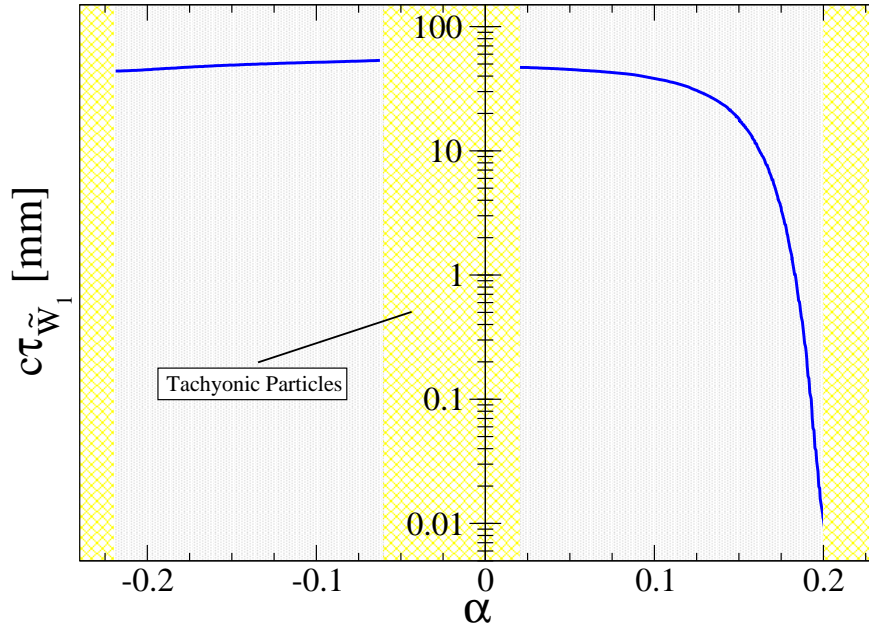


Figure 3: Lifetime $c\tau_{\tilde{W}_1}$ in mm of the light chargino state versus α in the HCAMSB model for $m_{3/2} = 50$ TeV, $\tan\beta = 10$ and $\mu > 0$.

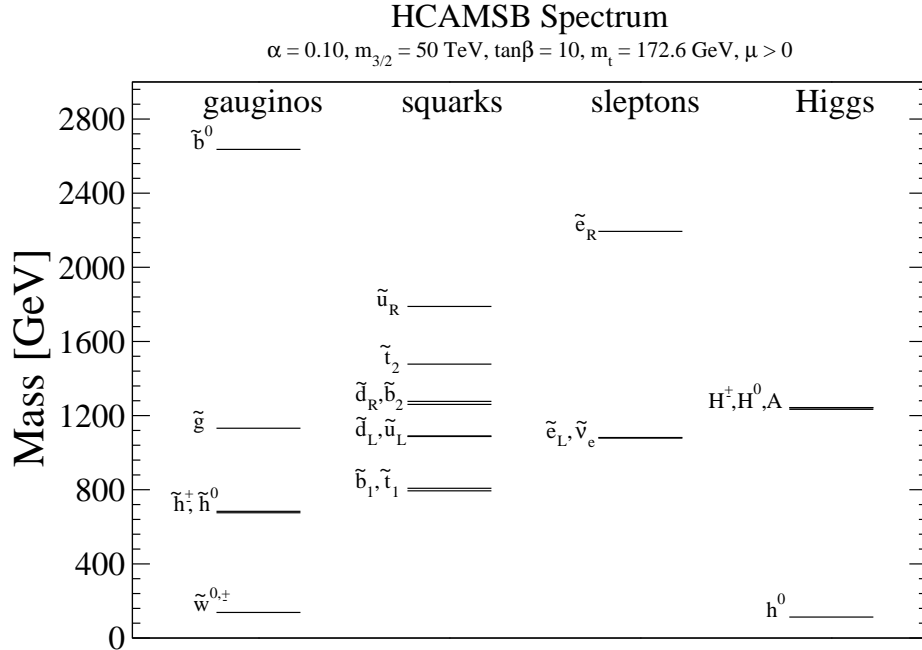
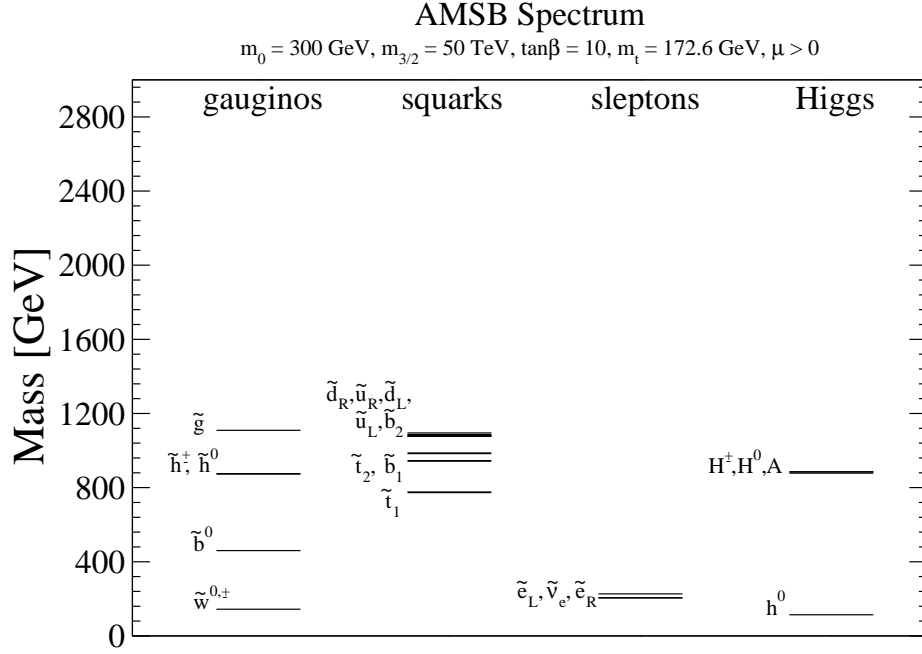


Figure 4: Mass spectra for mAMSB and HCAMSBS models with $m_{3/2} = 50 \text{ TeV}$, $\tan\beta = 10$ and $\mu > 0$. For mAMSB, we take $m_0 = 300 \text{ GeV}$, while for HCAMSBS, we take $\alpha = 0.1$.

bound on HCAMSB parameter space around $m_{3/2} \sim 30$ TeV.² The white-shaded regions all yield allowable superparticle mass spectra. The lowest value of $m_{\tilde{g}}$ which is accessible occurs at $m_{3/2} \sim 30$ TeV, where $m_{\tilde{g}} \sim 730$ GeV. This value is far beyond any reasonable reach of the Fermilab Tevatron, so instead we focus in this paper on HCAMSB signatures at the CERN LHC. For convenience, we also show in Fig. 5 contours of $m_{\tilde{g}}$ and $m_{\tilde{u}_L} = 1, 2$ and 3 TeV, and also contours of $m_{\tilde{t}_1} = 500$ and 1000 GeV, and $m_{\tilde{e}_L} = 350$ GeV. The region with $m_{\tilde{e}_L} \lesssim 350$ GeV may be accessible to probes of direct slepton pair production at the LHC[19].

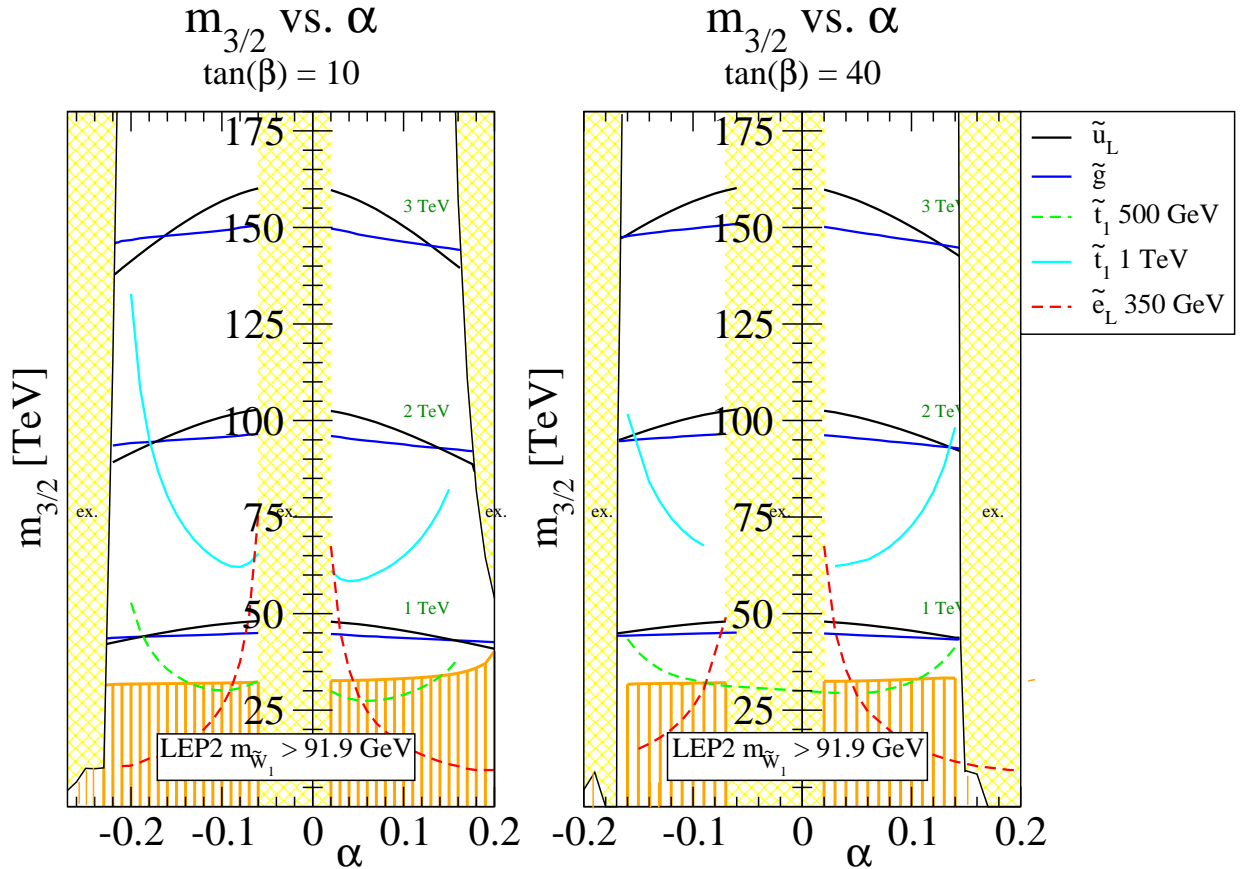


Figure 5: Allowed parameter space in the $m_{3/2}$ vs. α plane in the HCAMSB model with $\mu > 0$, $m_t = 172.6$ GeV and a). $\tan \beta = 10$ and b). $\tan \beta = 40$. We also show contours of $m_{\tilde{u}_L}$, $m_{\tilde{g}}$, $m_{\tilde{e}_L}$ and $m_{\tilde{t}_1}$.

²The LEP2 limit that $m_{H_{SM}} > 114.4$ GeV is also possibly constraining. However, we expect a theory error of $\sim \pm 3$ GeV on our calculated value of m_h . Since $m_h \gtrsim 111$ GeV throughout the plot, we do not adopt any constraint due to the Higgs mass.

2.2 $BF(b \rightarrow s\gamma)$ and $(g - 2)_\mu$ in HCAMSB

There also exist indirect limits on model parameter space from comparing measured values of $BF(b \rightarrow s\gamma)$ and $\Delta a_\mu \equiv (g - 2)_\mu$ against SUSY model predictions. As an example, we show in Fig. 6 the branching fraction for $BF(b \rightarrow s\gamma)$ in the HCAMSB model versus α for $m_{3/2} = 50$ and 100 TeV, and for $\tan\beta = 10$ and 40 (calculated using the Isatools subroutine ISABSG[20]). We also show the region between the blue horizontal lines as the SM prediction ($BF(b \rightarrow s\gamma)_{SM} = (3.15 \pm 0.23) \times 10^{-4}$ by a recent evaluation by Misiak[21]), and the region between the black-dotted lines as the region allowed by experiment[22].³ The red-dashed curves show the HCAMSB prediction. We see that in each of the frames there exists some region of at least near agreement with experiment. In frame b). with $m_{3/2} = 50$ TeV and $\tan\beta = 40$, the low α region leads to too high of a BF, while in frames a)., b). and d)., very high values of α lead to too small a BF.

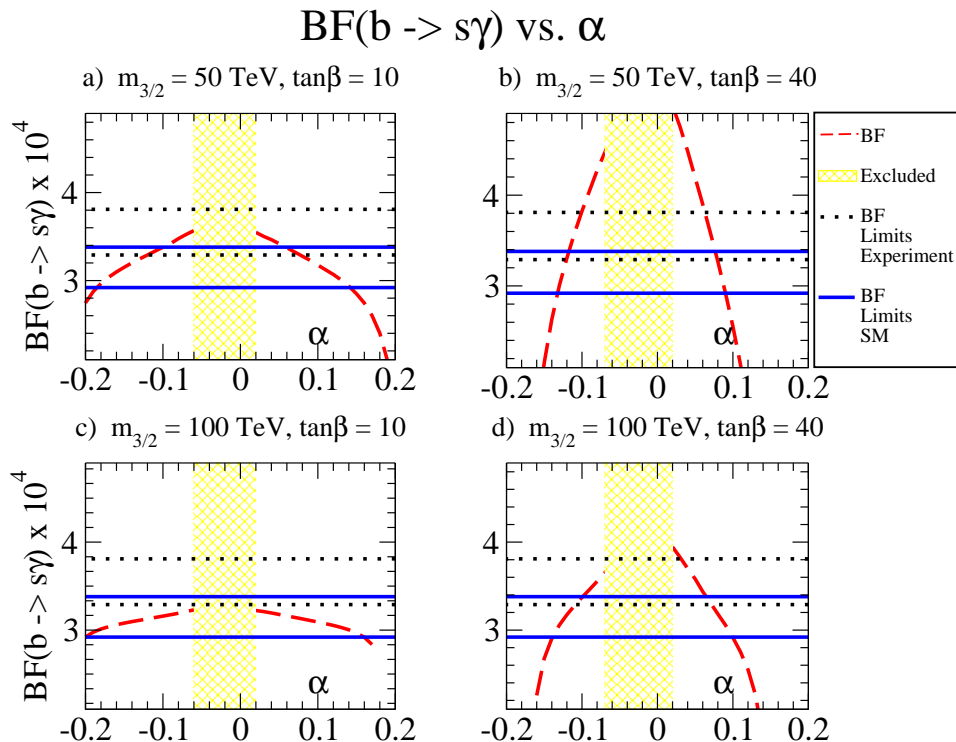


Figure 6: Branching fraction for $b \rightarrow s\gamma$ versus α in the HCAMSB model for $\mu > 0$ and $(m_{3/2}, \tan\beta) = a)$. (50 TeV, 10), $b)$. (50 TeV, 40), $c)$. (100 TeV, 10) and $d)$. (100 TeV, 40). We also take $m_t = 172.6$ GeV.

In Fig. 7, we plot the SUSY contribution to Δa_μ : Δa_μ^{SUSY} (using ISAGM2 from Isatools[23]). The contribution is large when α is small; in this case, rather light $\tilde{\mu}_L$ and $\tilde{\nu}_{\mu L}$ masses lead to

³ The branching fraction $BF(b \rightarrow s\gamma)$ has been measured by the CLEO, Belle and BABAR collaborations; a combined analysis[22] finds the branching fraction to be $BF(b \rightarrow s\gamma) = (3.55 \pm 0.26) \times 10^{-4}$.

large deviations from the SM prediction. It is well-known that there is a discrepancy between the SM predictions for Δa_μ , where τ decay data, used to estimate the hadronic vacuum polarization contribution to Δa_μ , gives rough accord with the SM, while use of $e^+e^- \rightarrow \text{hadrons}$ data at very low energy leads to a roughly 3σ discrepancy.

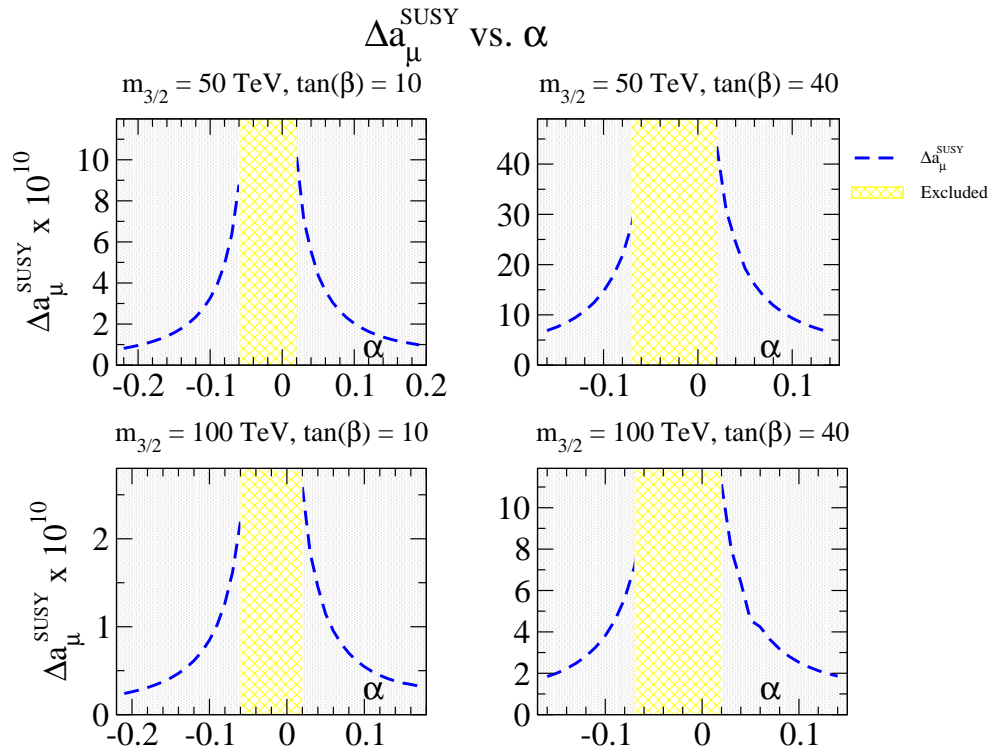


Figure 7: SUSY contribution to Δa_μ versus α in the HCAMSB model for $\mu > 0$ and $(m_{3/2}, \tan\beta) = a$. (50 TeV, 10), b). (50 TeV, 40), c). (100 TeV, 10) and d). (100 TeV, 40). We also take $m_t = 172.6$ GeV.

Finally, we remark upon the relic density of dark matter in the HCAMSB model. If thermal production of the lightest neutralino is assumed to give the dominant DM in the universe, then all over parameter space, the predicted neutralino abundance $\Omega_{\tilde{Z}_1} h^2$ is far below the WMAP measured value of $\Omega_{CDM} h^2 \sim 0.11$. Some sample calculated values are listed in Table 1. It has been suggested in Ref. [24] that production and decay of moduli fields or other processes can contribute to the DM abundance. Decay of moduli fields in the early universe could then account for the discrepancy between the measured DM abundance and the predicted thermal abundance in HCAMSB models. As an alternative, if the strong CP problem is solved via the Peccei-Quinn mechanism, then a superfield containing the axion/axino multiplet should occur. In this case, a mixture of axions[25] and axinos[26], rather than wino-like neutralinos, could constitute the DM abundance[27]. In light of these two alternative DM mechanisms, we regard the HCAMSB parameter space as essentially unconstrained by the measured abundance of DM in the universe.

3 HCAMSB at the LHC

3.1 Cross sections and branching fractions

Across almost all of the HCAMSB model parameter space, we expect \widetilde{W}_1 and \widetilde{Z}_1 to be wino-like, with $m_{\widetilde{W}_1} \simeq m_{\widetilde{Z}_1} \sim \frac{1}{7.7} m_{\widetilde{g}}$. Thus, for the HCAMSB model, the dominant sparticle production cross sections at the LHC will consist of the $pp \rightarrow \widetilde{W}_1^+ \widetilde{W}_1^- X$ and $pp \rightarrow \widetilde{W}_1^\pm \widetilde{Z}_1 X$ reactions (as noted at the bottom of Table 1). These reactions will be very difficult– if not impossible– to observe, since they yield no energetic calorimeter deposition to serve as a trigger at LHC detectors. Instead, sparticle detection prospects will have to rely on gluino and squark pair production to yield observable collider events.

At the lowest allowed values of $m_{3/2} \sim 30$ TeV, the gluino mass $m_{\widetilde{g}} \sim 730$ GeV, and the combined $\widetilde{g}\widetilde{g}$, $\widetilde{g}\widetilde{q}$ and $\widetilde{q}\widetilde{q}$ pair production cross sections are of order $10^3 - 10^4$ fb[14]. At low α values, the value of $m_{\widetilde{g}}$ is similar to $m_{\widetilde{q}_L}$ and $m_{\widetilde{q}_R}$ and all three of the above final states occur at similar rates. In the high α regime of HCAMSB, the right squarks become quite heavy, while third generation squark masses \widetilde{t}_1 and \widetilde{b}_1 become lighter. In this case, $\widetilde{g}\widetilde{g}$ and $\widetilde{g}\widetilde{u}_L$ or $\widetilde{g}\widetilde{c}_L$ can occur at observable rates, although the bulk of the strong production cross section can be dominated by $\widetilde{t}_1\widetilde{t}_1$ and $\widetilde{b}_1\widetilde{b}_1$ production. Since the \widetilde{t}_1 and \widetilde{b}_1 are dominantly left squarks at large α , and are elements of a doublet, their masses are nearly equal, and their production cross sections are similar. The direct $\widetilde{b}_1\widetilde{b}_1$ production cross section is shown in Fig. 8 for pp collisions at $\sqrt{s} = 14$ TeV[28].⁴ The stop pair production rate is nearly identical since $m_{\widetilde{b}_1} \simeq m_{\widetilde{t}_1}$.

At low values of α , since $m_{\widetilde{u}_R, \widetilde{c}_R} > m_{\widetilde{g}}$, we get $\widetilde{u}_R \rightarrow u\widetilde{g}$ and $\widetilde{c}_R \rightarrow c\widetilde{g}$ adding to the gluino production rate. The \widetilde{g} decays mainly into $b\widetilde{b}_1 + c.c.$ and $t\widetilde{t}_1 + c.c.$ states, with a subdominant fraction of decays into other $q\widetilde{q}_L$ pairs. As α increases, the right-squark masses increase, and ultimately decouple from the theory, while left-squark masses increase slightly to values just above $m_{\widetilde{g}}$. Thus, at high α , the \widetilde{g} state decays purely into $b\widetilde{b}_1 + c.c.$ and $t\widetilde{t}_1 + c.c.$ pairs. We then expect that if strongly interacting sparticle states of the HCAMSB model are accessible to LHC searches, they should yield events with a high multiplicity of b -quarks, t -quarks and \widetilde{b}_1 and \widetilde{t}_1 squarks, for all values of α .

In Fig. 9 and Fig. 10, we show the \widetilde{t}_1 and \widetilde{b}_1 branching fractions versus α for $m_{3/2} = 50$ TeV, $\tan\beta = 10$ and $\mu > 0$. At low values of α , we expect $\widetilde{t}_1 \rightarrow b\widetilde{W}_1$ at $\sim 67\%$ and $\widetilde{t}_1 \rightarrow t\widetilde{Z}_1$ at $\sim 33\%$. Similarly, at low α we expect $\widetilde{b}_1 \rightarrow t\widetilde{W}_1$ at $\sim 67\%$ and $\widetilde{b}_1 \rightarrow b\widetilde{Z}_1$ at $\sim 33\%$. As $|\alpha|$ increases, the value of $|\mu|$ decreases, until it becomes comparable to the gaugino mass M_2 , and the \widetilde{Z}_1 state becomes mixed wino-higgsino. As $|\mu|$ decreases, so do the \widetilde{Z}_2 , \widetilde{Z}_3 and \widetilde{W}_2 eigenstates masses (while $m_{\widetilde{Z}_4}$ increases with mass $\sim M_1$ as it is nearly pure bino-like). Thus, we see at large $|\alpha|$, decay modes such as $\widetilde{b}_1 \rightarrow b\widetilde{Z}_2$, $b\widetilde{Z}_3$ and $t\widetilde{W}_2$ turn-on, leading to more complex cascade decays. Also, as $|\alpha|$ gets large, the modes $\widetilde{t}_1 \rightarrow t\widetilde{Z}_2$, $t\widetilde{Z}_3$ and $b\widetilde{W}_2$ become accessible (though never dominant). Ultimately, as $|\alpha|$ increases even further, the values of $m_{\widetilde{t}_1}$ and $m_{\widetilde{b}_1}$ decrease, and the decay modes such as $\widetilde{t}_1 \rightarrow t\widetilde{Z}_3$, $t\widetilde{Z}_2$ and $t\widetilde{Z}_1$ all become kinematically

⁴ Initial LHC turn-on energy is expected to be around $\sqrt{s} = 7 - 10$ TeV, with a gradual ramp-up towards $\sqrt{s} = 14$ TeV. Cross sections are of course model dependent, but generally we expect an increase in cross sections of a factor of 2-4 in going from $\sqrt{s} = 10$ TeV to $\sqrt{s} = 14$ TeV. For instance, the $\sigma(pp \rightarrow t\bar{t}X)$ increases by a factor of 2.4 during this transition[29].

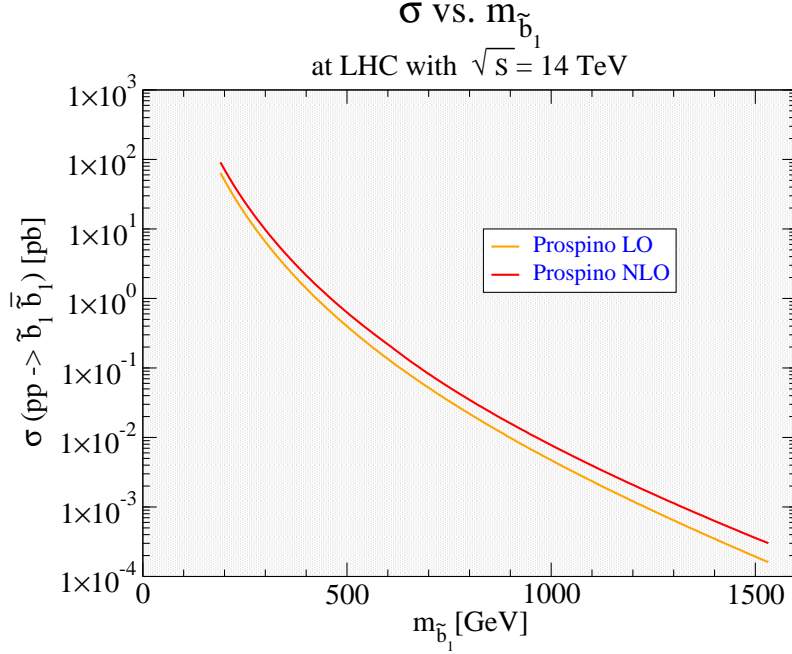


Figure 8: Cross section for $pp \rightarrow \tilde{b}_1 \bar{\tilde{b}}_1 X$ versus $m_{\tilde{b}_1}$ at LHC energy $\sqrt{s} = 14$ TeV).

suppressed. In fact, at the highest α values, the decay mode $\tilde{t}_1 \rightarrow b\tilde{W}_1$ becomes kinematically dis-allowed, so that decays such as $\tilde{t} \rightarrow b\ell\nu\tilde{Z}_1$ or $c\tilde{Z}_1$ then dominate.

In Fig's 11 and 12 we show the \tilde{t}_1 and \tilde{b}_1 branching fractions versus $m_{3/2}$ for a fixed value of $\alpha = 0.025$, $\tan\beta = 10$ and $\mu > 0$. Here we see that $\tilde{t}_1 \rightarrow b\tilde{W}_1$ and $t\tilde{Z}_1$ dominates out to large $m_{3/2}$ values. This behavior persists also for high α values. In the case of \tilde{b}_1 , we see $\tilde{b}_1 \rightarrow t\tilde{W}_1$ or $b\tilde{Z}_1$ dominates over the entire $m_{3/2}$ range as well.

Thus, in the HCAMSB model, we expect gluino and squark production events to cascade decay into third generation quarks and squarks. We then expect HCAMSB collider events to contain a high multiplicity of b -jets, along with isolated leptons from $t \rightarrow bW$ decays, and large E_T^{miss} from escaping \tilde{Z}_1 or ν states. Note as is usual in AMSB models with $m_{\tilde{W}_1} \sim m_{\tilde{Z}_1}$ that the \tilde{W}_1 is long-lived, and can fly distances of order millimeters to centimeters before decaying via $\tilde{W}_1^+ \rightarrow \pi^+\tilde{Z}_1$ into a soft pion. The presence of the highly ionizing chargino track, and its abrupt termination upon chargino decay, is characteristic of models such as mAMSB and HCAMSB where the gaugino mass M_2 is far lighter than M_1 and $|\mu|$.

3.2 Characteristics of LHC collider events for cases HCAMSB1 and HCAMSB2

We use Isajet 7.79[7] for the simulation of signal and background events at the LHC. A toy detector simulation is employed with calorimeter cell size $\Delta\eta \times \Delta\phi = 0.05 \times 0.05$ and $-5 < \eta < 5$. The hadronic calorimeter (HCAL) energy resolution is taken to be $80\%/\sqrt{E} + 3\%$ for $|\eta| < 2.6$

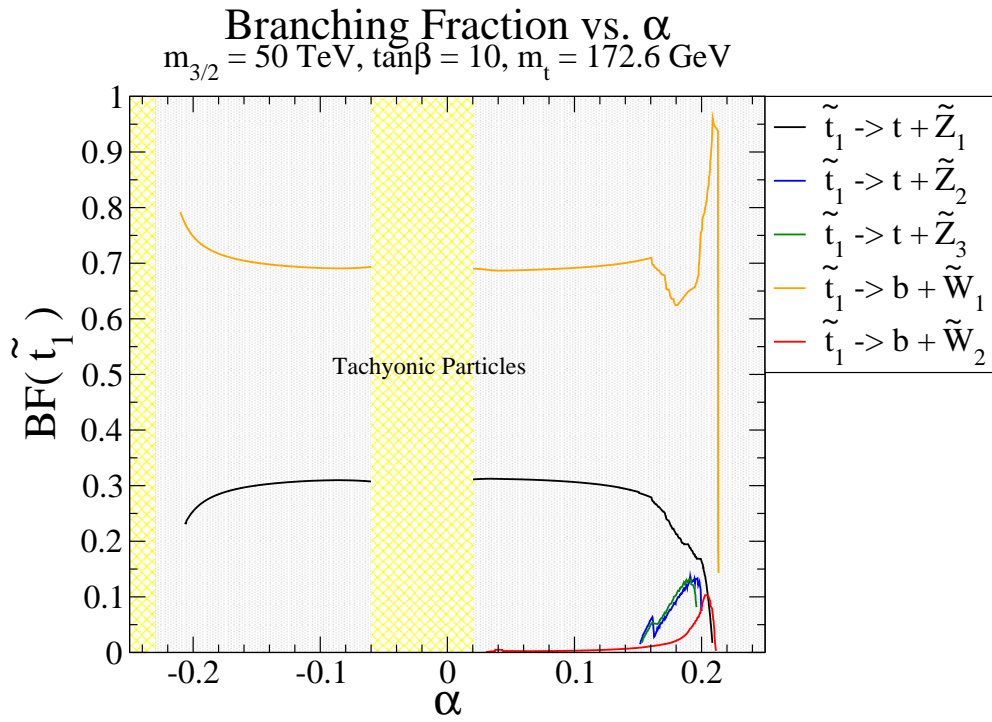


Figure 9: Branching fraction of \tilde{t}_1 versus α for $m_{3/2} = 50 \text{ TeV}$, $\tan\beta = 10$ and $\mu > 0$.

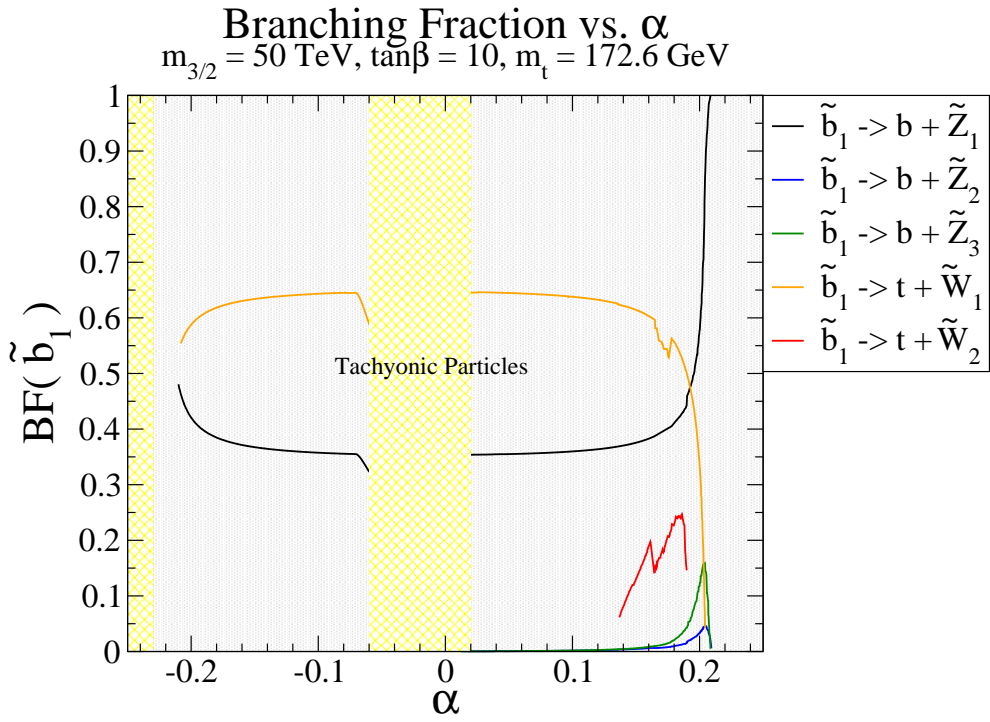


Figure 10: Branching fraction of \tilde{b}_1 versus α for $m_{3/2} = 50 \text{ TeV}$, $\tan\beta = 10$ and $\mu > 0$.

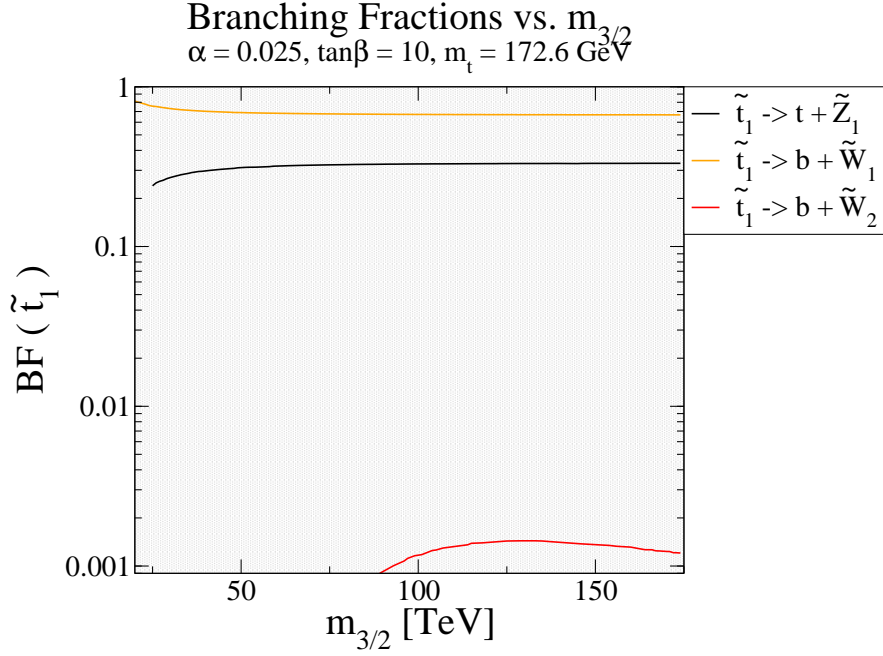


Figure 11: Branching fraction of \tilde{t}_1 versus $m_{3/2}$ for $\alpha = 0.025$, $\tan\beta = 10$ and $\mu > 0$.

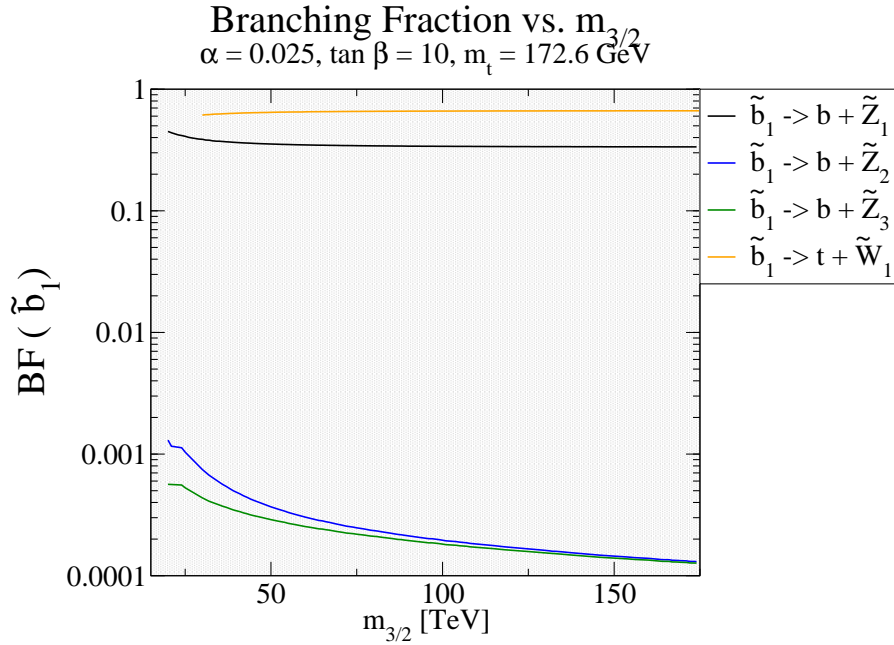


Figure 12: Branching fraction of \tilde{b}_1 versus $m_{3/2}$ for $\alpha = 0.025$, $\tan\beta = 10$ and $\mu > 0$.

and forward calorimeter (FCAL) is $100\%/\sqrt{E} + 5\%$ for $|\eta| > 2.6$. The electromagnetic (ECAL) energy resolution is assumed to be $3\%/\sqrt{E} + 0.5\%$. We use the UA1-like jet finding algorithm GETJET with jet cone size $R = 0.4$ and require that $E_T(\text{jet}) > 50$ GeV and $|\eta(\text{jet})| < 3.0$. Leptons are considered isolated if they have $p_T(e \text{ or } \mu) > 20$ GeV and $|\eta| < 2.5$ with visible activity within a cone of $\Delta R < 0.2$ of $\Sigma E_T^{\text{cells}} < 5$ GeV. The strict isolation criterion helps reduce multi-lepton backgrounds from heavy quark ($c\bar{c}$ and $b\bar{b}$) production.

We identify a hadronic cluster with $E_T > 50$ GeV and $|\eta(j)| < 1.5$ as a b -jet if it contains a B hadron with $p_T(B) > 15$ GeV and $|\eta(B)| < 3$ within a cone of $\Delta R < 0.5$ about the jet axis. We adopt a b -jet tagging efficiency of 60%, and assume that light quark and gluon jets can be mis-tagged as b -jets with a probability $1/150$ for $E_T < 100$ GeV, $1/50$ for $E_T > 250$ GeV, with a linear interpolation for $100 \text{ GeV} < E_T < 250 \text{ GeV}$ [30].

We have generated 2M events each for cases HCAMSB1 and HCAMSB2 from Table 1. In addition, we have generated background events using Isajet for QCD jet production (jet-types include g, u, d, s, c and b quarks) over five p_T ranges as shown in Table 2[31]. Additional jets are generated via parton showering from the initial and final state hard scattering subprocesses. We have also generated backgrounds in the $W + jets, Z + jets, t\bar{t}(172.6)$ and WW, WZ, ZZ channels at the rates shown in the same Table. The $W + jets$ and $Z + jets$ backgrounds use exact matrix elements for one parton emission, but rely on the parton shower for subsequent emissions.

For our initial selection of signal events, we first require the following cuts labeled **C1**:

- $n(\text{jets}) \geq 4$,
- $E_T^{\text{miss}} > \max(100 \text{ GeV}, 0.2M_{eff})$
- $E_T(j1, j2, j3, j4) > 100, 50, 50, 50 \text{ GeV}$,
- transverse sphericity $S_T > 0.2$,

where $M_{eff} = E_T^{\text{miss}} + E_T(j1) + E_T(j2) + E_T(j3) + E_T(j4)$.

In Fig. 13, we plot the resulting distribution in jet multiplicity (after relaxing the $n(\text{jets}) \geq 4$ requirement). We see that the signal distributions for cases HCAMSB1 and HCAMSB2 are harder than the summed background histogram (gray), although signal doesn't exceed BG until very high jet multiplicities around $n(\text{jets}) \sim 9$. Thus, selecting signal events with $n(\text{jets}) \geq 2 - 4$ should be beneficial.

In Fig. 14, we plot the distribution in b -jet multiplicity from cases HCAMSB1 and HCAMSB2 against summed SM BG after cuts **C1** (while again relaxing $n(\text{jets}) \geq 4$). As expected, the signal distributions are harder than the summed BG owing to the large number of b and t quarks produced in the HCAMSB cascade decay events. Signal typically exceeds BG around $n(b\text{-jets}) \sim 5$. Thus, requiring the presence of at least one identified b -jet will aide in selecting HCAMSB signal over BG.

In Fig. 15, we show the distribution in isolated lepton multiplicity after cuts **C1**. In this case, we see HCAMSB1, with its much lighter spectrum of sleptons, gives a much harder distribution in $n(\text{leptons})$ than HCAMSB2. By $n(\ell) = 3$, signal far exceeds BG, especially for case HCAMSB1, where signal remains around 5 fb. This case should already be visible in early LHC SUSY searches with just a few fb^{-1} of integrated luminosity[32].

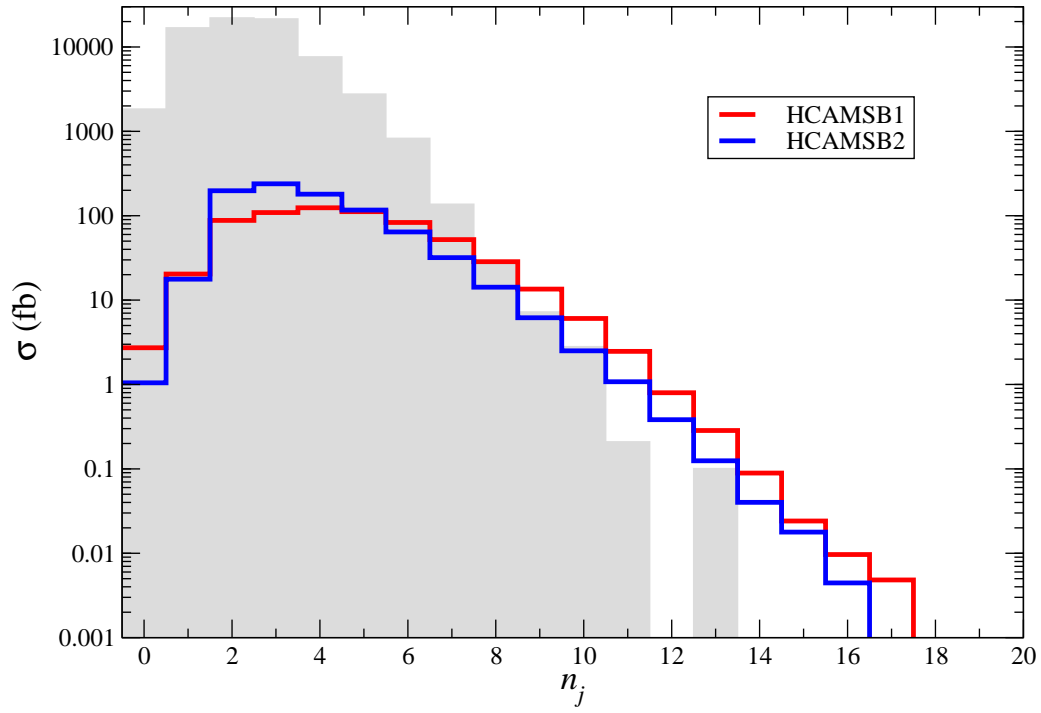


Figure 13: Distribution in jet multiplicity in LHC collider events with $\sqrt{s} = 14$ TeV from cases HCAMSB1 (red), HCAMSB2 (blue), and summed SM background (grey), after cuts set $C1$.

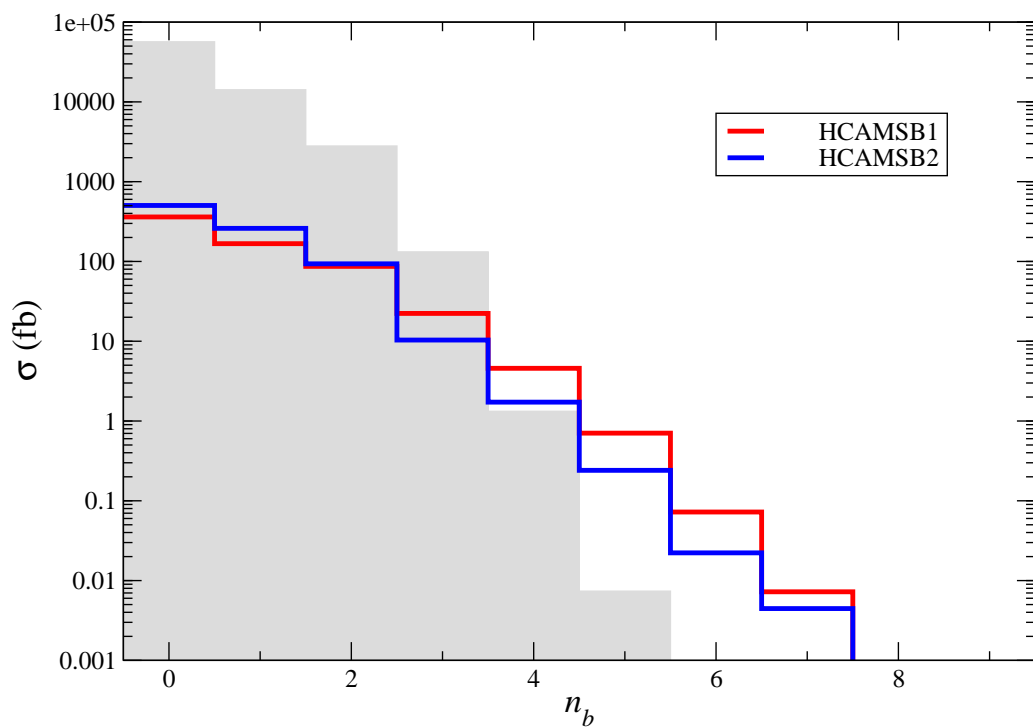


Figure 14: Distribution in b -jet multiplicity in LHC collider events with $\sqrt{s} = 14$ TeV from cases HCAMSB1 (red), HCAMSB2 (blue), and summed SM background (grey), after cuts set $C1$.

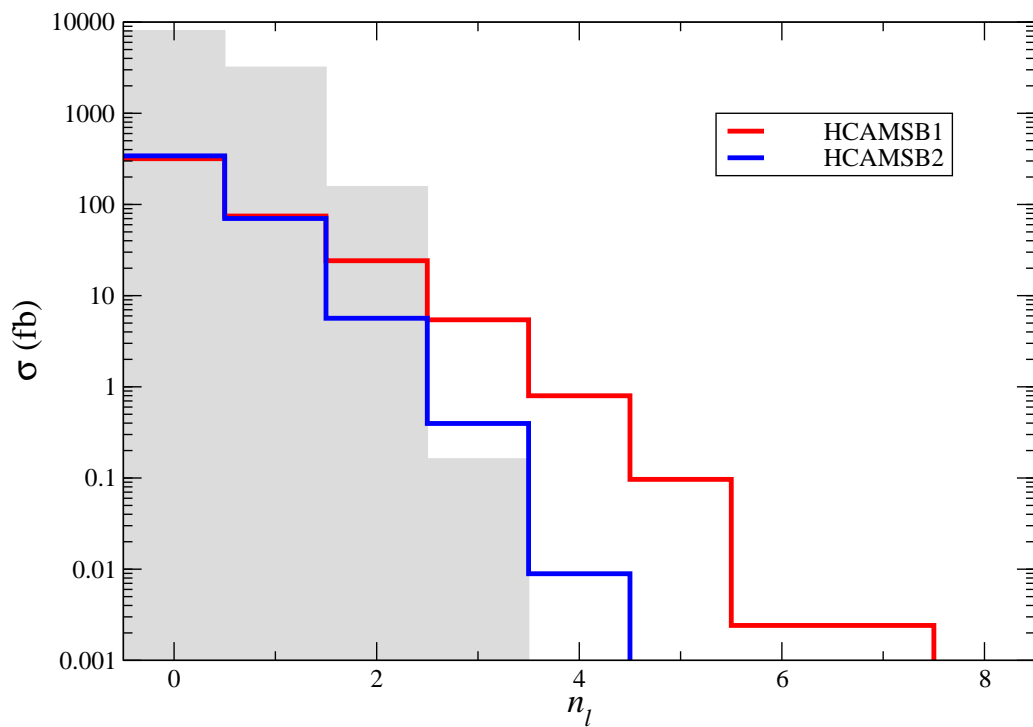


Figure 15: Distribution in isolated lepton multiplicity in LHC collider events with $\sqrt{s} = 14$ TeV from cases HCAMSB1 (red), HCAMSB2 (blue), and summed SM background (grey), after cuts set $\mathcal{C}1$.

Fig. 16 shows the distribution in E_T of *a*). the hardest jet and *b*). the second hardest jet in HCAMSB1 and HCAMSB2 events, along with SM BG after cuts $C1$ (but where the hardest jet $E_T(j1) > 100$ GeV cut is relaxed). Here, the case HCAMSB2 peaks around $E_T(j1) \sim 150$ GeV, due mainly to $\tilde{b}_1\tilde{\bar{b}}_1$ production followed by $\tilde{b} \rightarrow b\tilde{Z}_1$ decay. Signal begins to exceed BG by around 450 GeV (HCAMSB1) or 550 GeV (HCAMSB2).

In Fig. 17, we show the missing E_T distribution from signal and BG events. The distribution from HCAMSB2, which is dominated by relatively light 3rd generation squark production, is considerably softer than HCAMSB1, where production of TeV-scale squarks and gluinos is dominant. Both cases exceed the summed BG for $E_T^{\text{miss}} \gtrsim 500$ GeV.

We show in Fig. 18 the distribution in augmented effective mass $A_T = E_T^{\text{miss}} + \sum E_T(\text{jets}) + \sum E_T(\text{isol. leptons})$. In this case, signal point HCAMSB1 yields a rather smooth, hard distribution which emerges from BG around $A_T \sim 1600$ GeV. Meanwhile, the A_T distribution from case HCAMSB2 actually resolves itself into two components: a soft component peaks around $A_T \sim 750$ GeV, and is due to 3rd generation squark pair production. The harder component, peaking around $A_T \gtrsim 2000$ GeV, occurs due to \tilde{g} and \tilde{q}_L production.

3.2.1 LHC cascade decay events including HITs: a smoking gun for AMSB models

Of course, a distinctive property of models like HCAMSB (and also mAMSB) with a wino-like \tilde{Z}_1 state is that the chargino is very long lived, as shown in Fig. 3. Thus, once we have obtained cascade decay signal events in any of the multi-jet plus multi-lepton plus E_T^{miss} channels, we may in addition look for the presence of a highly-ionizing track (HIT) from the long-lived chargino. The presence of HITs in the SUSY collider events would be indicative of models such as mAMSB or HCAMSB, where $M_2 \ll M_1$ and M_3 , so that the lightest neutralino is a nearly pure wino state and where $m_{\tilde{W}_1} \simeq m_{\tilde{Z}_1}$.

3.2.2 Cascade decays including HITs plus $Z \rightarrow \ell\bar{\ell}$: a smoking gun for HCAMSB?

Next we examine the distribution in $m(\ell^+\ell^-)$ for cascade decay events containing two same-sign isolated dileptons (here, $\ell = e$ or μ). This distribution has for long been touted as being very useful as a starting point for reconstructing sparticle masses in SUSY cascade decay events, because it may contain a kinematic mass edge from $\tilde{Z}_2 \rightarrow \tilde{\ell}^\pm\ell^\mp$ or $\tilde{Z}_2 \rightarrow \ell^+\ell^-\tilde{Z}_1$ decays. In the case of mAMSB models, such a mass edge may be present because \tilde{Z}_2 is bino-like and can decay into $\tilde{\ell}_R^\pm\ell^\mp$ at a high rate. In the case of HCAMSB models, the \tilde{Z}_2 state (and also the \tilde{Z}_3 state) is expected to be rather heavy and higgsino-like; it decays mainly into two-body modes such as $\tilde{Z}_2 \rightarrow \tilde{W}_1^\pm W^\mp$, $\tilde{Z}_1 h$ and $\tilde{Z}_2 \rightarrow \tilde{Z}_1 Z$. In particular, the later decay should always be open (except when $\mu \rightarrow 0$ at the very highest α values) and can occur with branching fractions at the tens of percent level (see Table 1). However, in mAMSB models, where \tilde{Z}_2 is bino-like, its decay to $\tilde{Z}_1 Z$ is highly suppressed due to the structure of the $\tilde{Z}_1\tilde{Z}_2 Z$ coupling (see Eq. 8.101 of Ref. [14]). Thus, we would expect in HCAMSB models, instead of kinematic mass edges, a continuum distribution in OS dilepton invariant mass, with a visible peak at $m(\ell^+\ell^-) \sim M_Z$. In Fig. 19, we show the resulting distribution using cuts $C1$ plus $A_T > 1500$ GeV, to reduce SM BGs. As expected, the signal stands out well above SM BG, but as a continuum, with a Z peak. This distribution might serve as a ‘‘smoking gun’’ LHC signature for HCAMSB

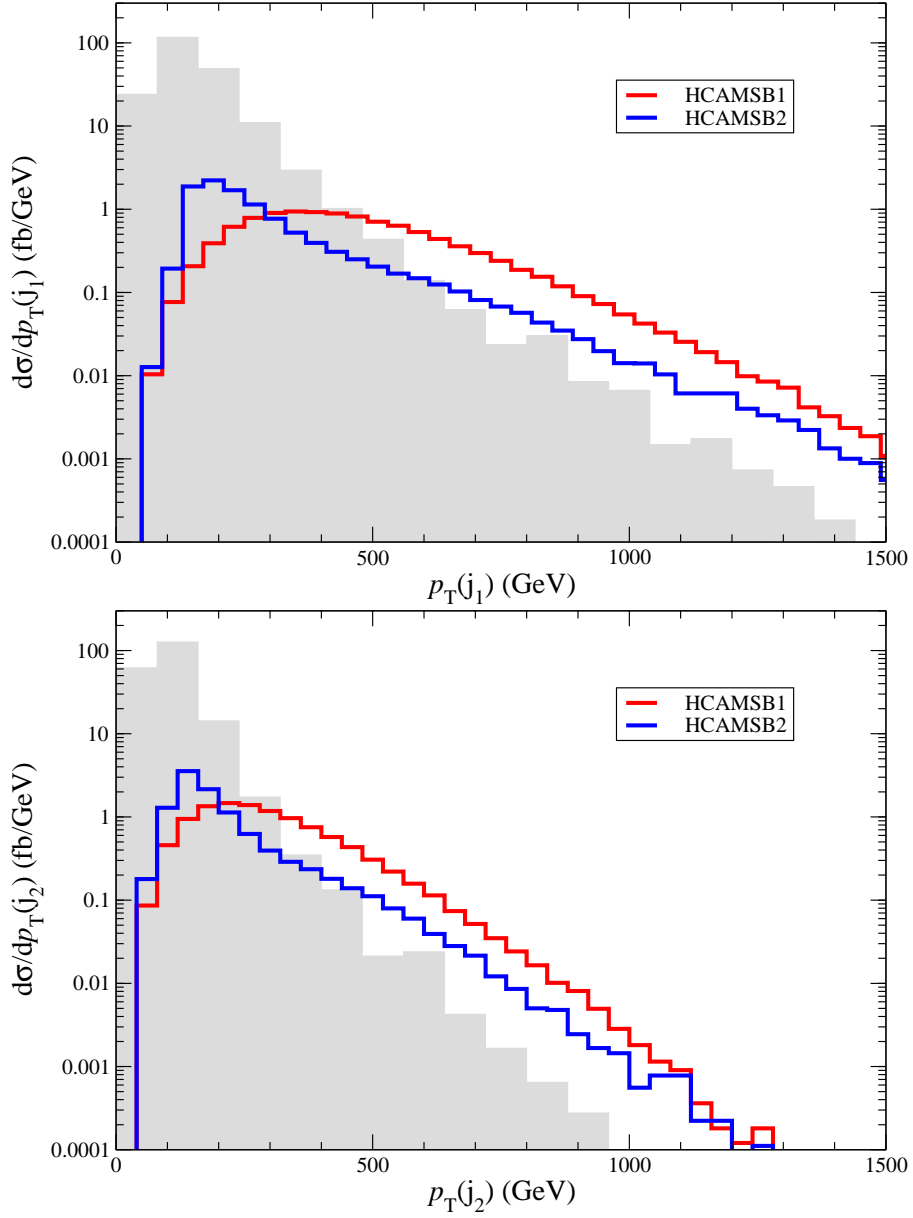


Figure 16: Distribution in *a*). hardest jet E_T and *b*). second hardest jet E_T in LHC collider events with $\sqrt{s} = 14$ TeV from cases HCAMSB1 (red), HCAMSB2 (blue), and summed SM background (grey), after cuts set $C1$.

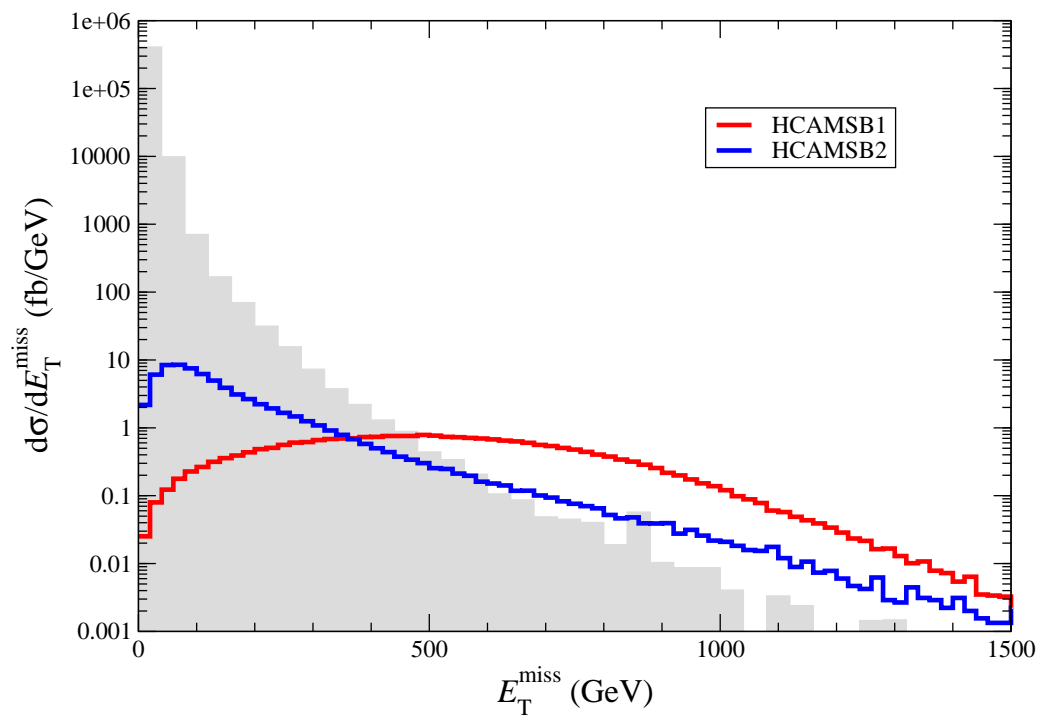


Figure 17: Distribution in missing E_T from LHC collider events with $\sqrt{s} = 14$ TeV from cases HCAMSB1 (red), HCAMSB2 (blue), and summed SM background (grey), after cuts set $C1$.

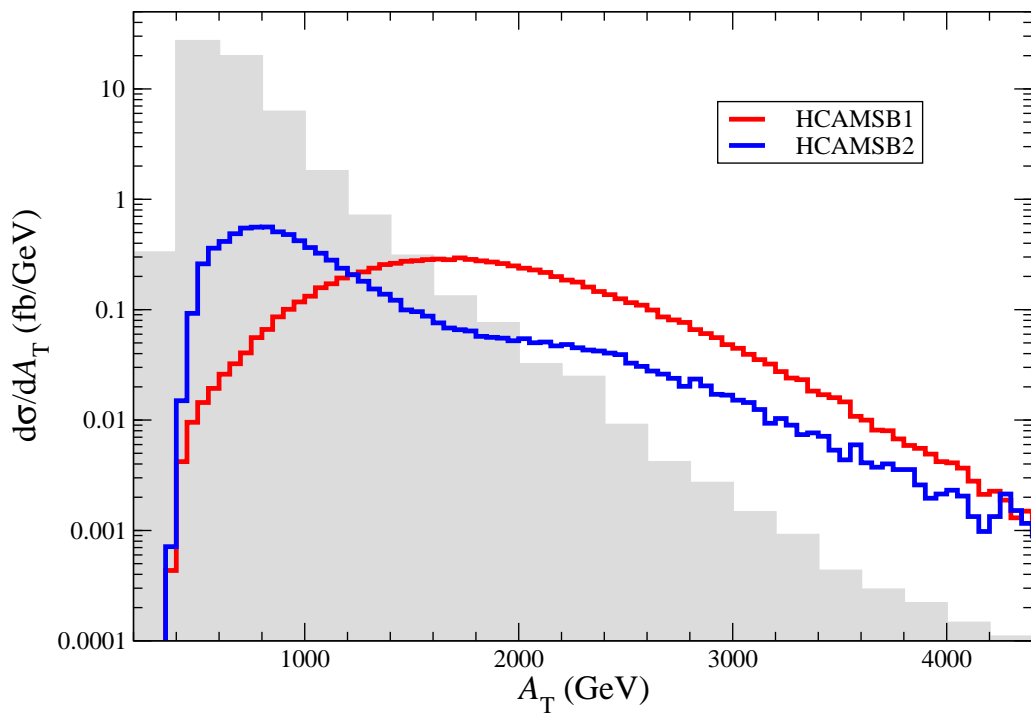


Figure 18: Distribution in augmented effective mass A_T from LHC collider events with $\sqrt{s} = 14$ TeV from cases HCAMSB1 (red), HCAMSB2 (blue), and summed SM background (grey), after cuts set $C1$.

models: we would expect– in the case of HCAMSB models at the LHC– cascade decay events with occasional HITs from the wino-like late-decaying charginos, but also with an OS dilepton spectrum with a discernable $Z \rightarrow \ell^+\ell^-$ peak! In mAMSB at high values of $\tan\beta$, mixing effects in the neutralino sector can also allow for some $Z \rightarrow \ell^+\ell^-$ cascade decay events.

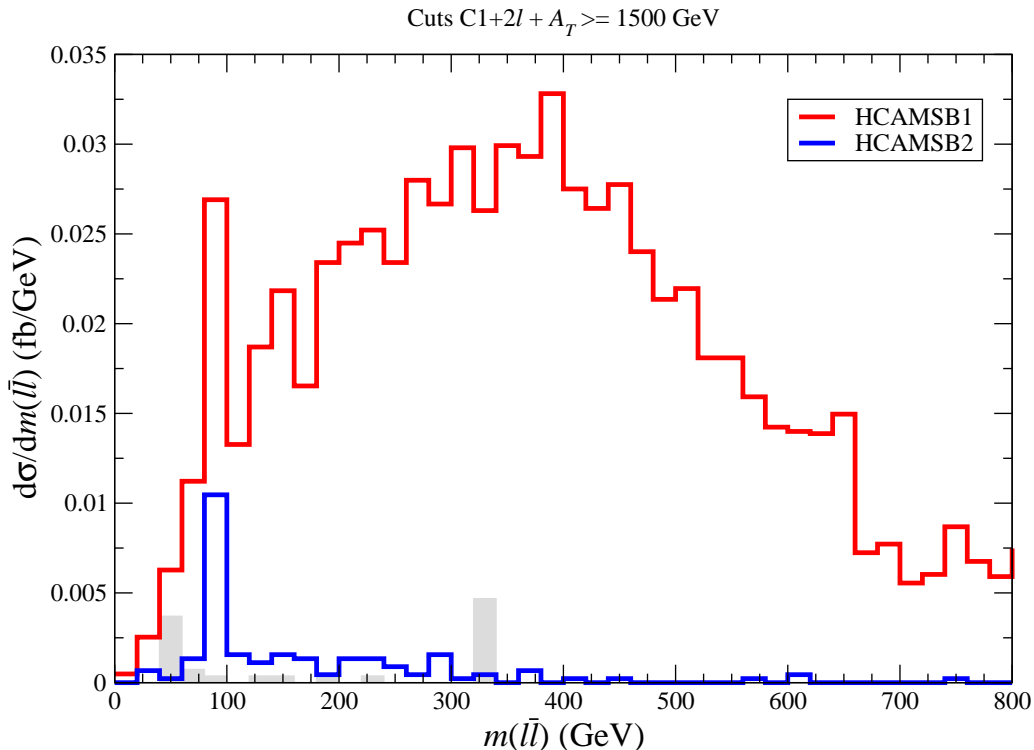


Figure 19: Invariant mass distribution for same-flavor/opposite sign dileptons from HCAMSB1 and HCAMSB2 after requiring cuts set $C1$ plus $A_T > 1500$ GeV.

3.3 The reach of LHC for two HCAMSB model lines

We would next like to investigate the reach of the CERN LHC for SUSY in the HCAMSB model. To this end, we will adopt two model lines. The first contains point HCAMSB1, and so has $\alpha = 0.025$, $\tan\beta = 10$ and $\mu > 0$. We will vary $m_{3/2}$ over the range 30 TeV to 200 TeV. For the second model line, we will take $\alpha = 0.15$. We must take α somewhat lower than the HCAMSB2 point, since for $\alpha = 0.195$, $m_{3/2}$ only extends up to about 60 TeV before hitting the EWSB-disallowed region (from Fig. 5). The sparticle mass spectra versus $m_{3/2}$ is shown for each of the two model lines in Fig. 20.

Motivated by the previous signal and background distributions, we will require the following cuts $C2$ [33]:

- $n(jets) \geq 2$
- $S_T > 0.2$

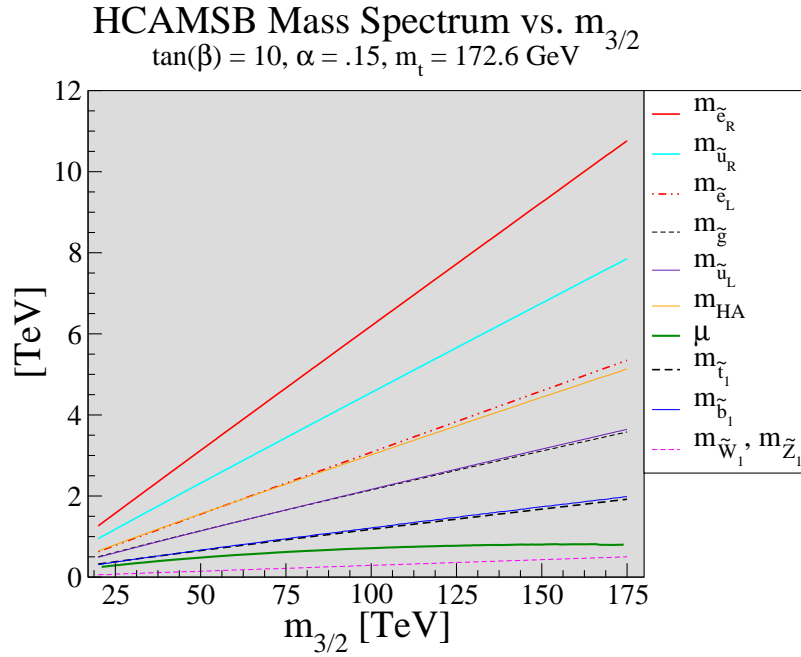
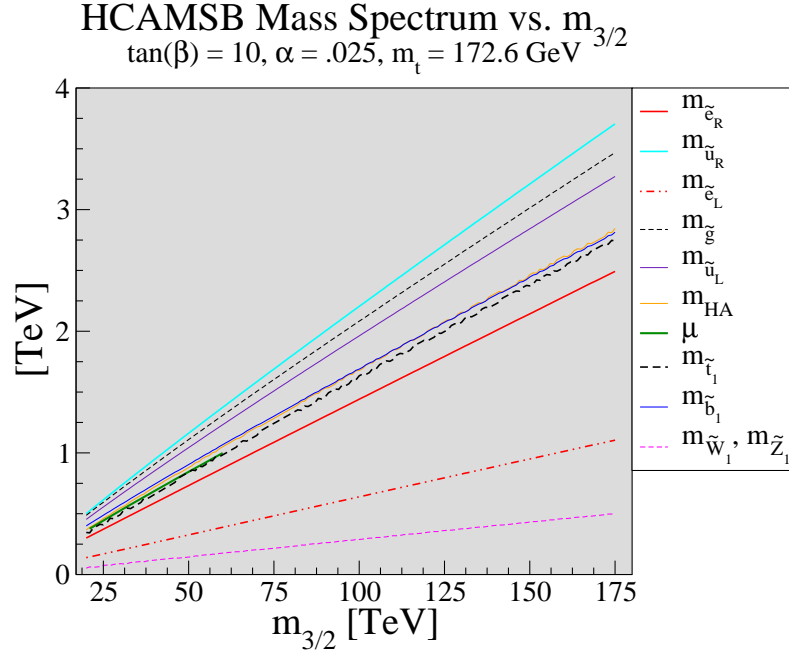


Figure 20: Sparticle mass spectrum versus $m_{3/2}$ for HCAMSB model with a). $\alpha = 0.025$ and b). $\alpha = 0.15$ for $\tan \beta = 10$, with $\mu > 0$ and $m_t = 172.6 \text{ GeV}$.

process	0ℓ	1ℓ	OS	SS	3ℓ
QCD(p_T : 0.05-0.10 TeV)	–	–	–	–	–
QCD(p_T : 0.10-0.20 TeV)	–	–	–	–	–
QCD(p_T : 0.20-0.40 TeV)	73.5	–	–	–	–
QCD(p_T : 0.40-1.00 TeV)	42.6	26.5	37.3	–	–
QCD(p_T : 1.00-2.40 TeV)	0.8	0.6	0.3	0.015	–
$t\bar{t}$	1253.2	341.2	224.9	0.25	0.25
$W + jets; W \rightarrow e, \mu, \tau$	60.6	5.6	2.8	–	–
$Z + jets; Z \rightarrow \tau\bar{\tau}, \nu s$	61.4	0.0	0.77	–	–
WW, ZZ, WZ	0.11	–	–	–	–
<i>summed SM BG</i>	1492.3	374.1	266.1	0.26	0.25
HCAMSB1	100.1	53.2	13.1	2.4	3.3
HCAMSB2	223.5	58.7	4.6	1.7	0.35

Table 2: Estimated SM background cross sections (plus two HCAMSB benchmark points) in fb for various multi-lepton plus jets + E_T^{miss} topologies after cuts C2 with $E_T^c = 100$ GeV.

- $n(b - jets) \geq 1$
- $E_T(j1), E_T(j2), E_T^{\text{miss}} > E_T^c,$

where E_T^c can be variable. Parameter space points with lower sparticle masses will benefit from lower choices of E_T^c , while points with heavier sparticle masses, lower cross sections but higher energy release per event, will benefit from higher choices of E_T^c . In addition, in the zero-leptons channel we require $30^\circ < \Delta\phi(\vec{E}_T^{\text{miss}}, \vec{E}_T(j_c)) < 90^\circ$ between the \vec{E}_T^{miss} and the nearest jet in transverse opening angle. For all isolated leptons ℓ , we require $p_T(\ell) > 20$ GeV, and for events with a single isolated lepton, we require the transverse mass $M_T(\ell, E_T^{\text{miss}}) \geq 100$ GeV to reject background events from $W \rightarrow \ell\nu_\ell$ production. We separate the signal event channels according to the multiplicity of isolated leptons: the 0ℓ , 1ℓ , same-sign (SS) and opposite-sign (OS) dilepton, and 3ℓ channels. We do not here require “same flavor” on the SS or OS dilepton events.

The resultant cross sections after cuts C2 for SM backgrounds along with signal points HCAMSB1 and HCAMSB2 are listed in Table 2 for $E_T^c = 100$ GeV. For each BG channel, we have generated ~ 2 million simulated events. With the hard cuts C2, we are unable to pick up BG cross sections in some of the multi-lepton channels. We will consider a signal to be observable at an assumed value of integrated luminosity if *i*) the signal to background ratio, $S/B \geq 0.2$, *ii*) the signal has a minimum of five events, and *iii*) the signal satisfies a statistical criterion $S \geq 5\sqrt{B}$ (a 5σ effect).

Using the above criteria, the 100 fb^{-1} reach of the LHC can be computed for each signal channel. In Fig. 21, we show the signal rates versus $m_{3/2}$ for each of the two model lines for $E_T^c = 100, 300$ and 500 GeV. The $5\sigma/5$ event, 100 fb^{-1} reach is denoted by the horizontal lines for each E_T^c value. We see the LHC reach in the 0ℓ channel extends to $m_{3/2} \sim 65, 105$ and 115 TeV for $E_T^c = 100, 300$ and 500 GeV, respectively, for the $\alpha = 0.025$ case. This corresponds to a reach in $m_{\tilde{g}}$ of 1.4, 2.2 and 2.4 TeV. The $\alpha = 0.15$ model, shown in frame b)., exhibits a 100

fb^{-1} reach of $m_{3/2} = 60, 100$ and 105 TeV for each E_T^c value, corresponding to a reach in $m_{\tilde{g}}$ of 1.3, 2.1 and 2.2 TeV, respectively. The reach for the high α model line is somewhat lower than the low α model line since many of the squark masses increase severely with α , and no longer contribute to the signal events.

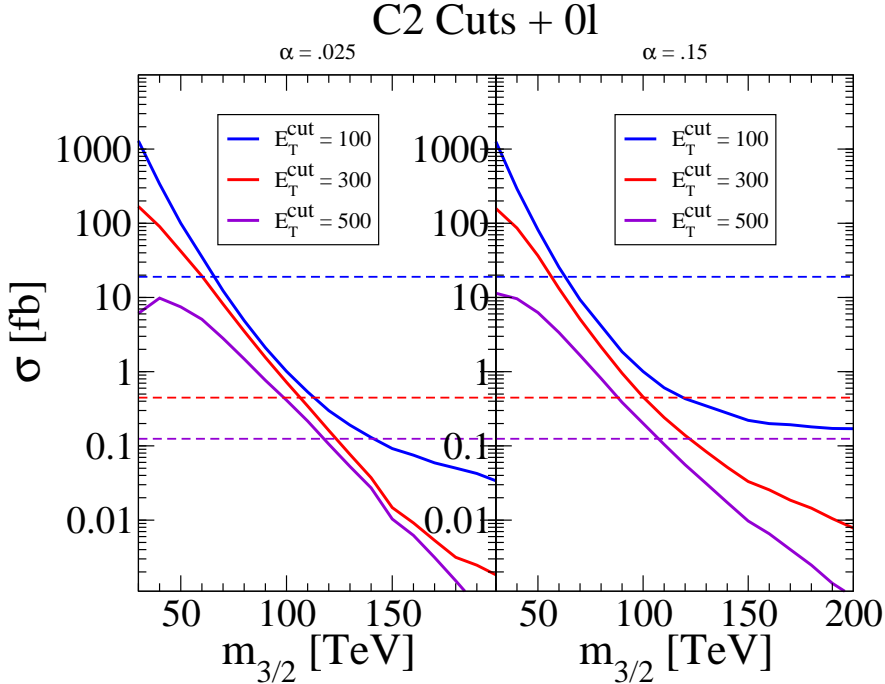


Figure 21: Cross section for multi-jet plus E_T^{miss} events with $n(\ell) = 0$ at the LHC after cuts $C2$ listed in the text with $E_T^c = 100, 300$ and 500 GeV, versus $m_{3/2}$, from HCAMSB model points with $\tan\beta = 10, \mu > 0$ and a). $\alpha = 0.025$ and b). $\alpha = 0.15$. We also list the $100 \text{ fb}^{-1} 5\sigma$ reach with the horizontal lines.

In Fig's 22-25, we show the corresponding 100 fb^{-1} reach of LHC for the two HCAMSB model lines in the $1\ell, OS, SS$ and 3ℓ channels. We do not exhibit a 5σ horizontal line for those cases where we generate no surviving background events. The reach in terms of $m_{3/2}$ for all channels is summarized in Table 3. For a given E_T^c value and signal channel, the upper entry corresponds to the $\alpha = 0.025$ model line, while the lower entry corresponds to the $\alpha = 0.15$ model line. By examining Table 3, we see that the maximal reach of LHC with 100 fb^{-1} for the $\alpha = 0.025$ model line occurs in the 3ℓ channel for $E_T^c = 100$ GeV, with $m_{3/2} \sim 80$ GeV being probed. However, a higher reach can be obtained by going to harder cuts with $E_T^c = 500$ GeV in the 0ℓ channel, where the reach extends to $m_{3/2} \sim 115$ GeV, corresponding to a reach in $m_{\tilde{g}}$ of ~ 2.4 TeV. The maximal LHC reach for the $\alpha = 0.15$ model line with $E_T^c = 100$ GeV occurs in the 1ℓ and SS dilepton channels, with $m_{3/2} = 65$ GeV being probed. The best reach for $\alpha = 0.15$ can be obtained using $E_T^c = 500$ GeV in the 0ℓ channel, where $m_{3/2} \sim 105$ TeV

can be probed, corresponding to a reach in $m_{\tilde{g}}$ of about 2.2 TeV.

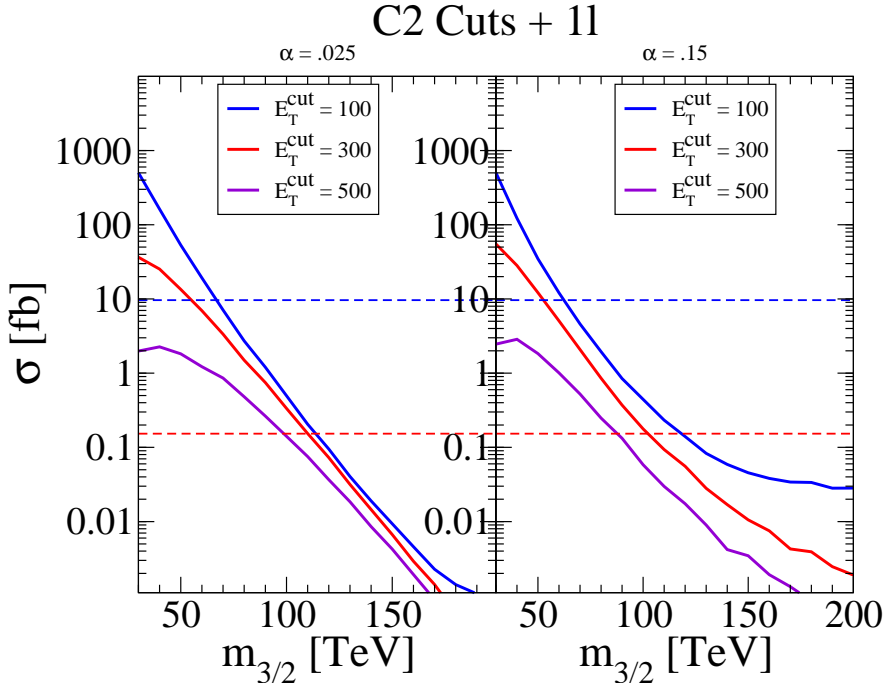


Figure 22: Cross section for multi-jet plus E_T^{miss} events with $n(\ell) = 1$ at the LHC after cuts $C2$ listed in the text with $E_T^c = 100, 300$ and 500 GeV, versus $m_{3/2}$, from HCAMSB model points with $\tan\beta = 10$, $\mu > 0$ and a). $\alpha = 0.025$ and b). $\alpha = 0.15$. We also list the 100 fb^{-1} 5σ reach with the horizontal lines.

4 Discussion and conclusions

In this paper, we have examined some phenomenological consequences of hypercharged anomaly-mediated SUSY breaking models at the LHC. We have computed the expected sparticle mass spectrum, and mapped out the relevant parameter space of the HCAMSB model. We have computed sparticle branching fractions, production cross sections and expected LHC collider events, and compared against expectations for SM backgrounds. Our main result was to compute the reach of the LHC for HCAMSB models assuming 100 fb^{-1} of integrated luminosity. We find an LHC reach to $m_{3/2} \sim 115$ TeV (corresponding to $m_{\tilde{g}} \sim 2.4$ TeV) for low values of α , and a reach to $m_{3/2} \sim 105$ TeV (corresponding to $m_{\tilde{g}} \sim 2.2$ TeV) for large α . We expect the reach for $\mu < 0$ to be similar to the reach for $\mu > 0$, due to similarities in the spectra for the two cases (see Fig. 1.) We also expect the reach for large $\tan\beta$ to be similar to the reach for low $\tan\beta$ in the 0ℓ and 1ℓ channels (differences in the multi-lepton channels can occur due to enhanced -ino decays to taus and bs at large $\tan\beta$). The LHC reach for HCAMSB models

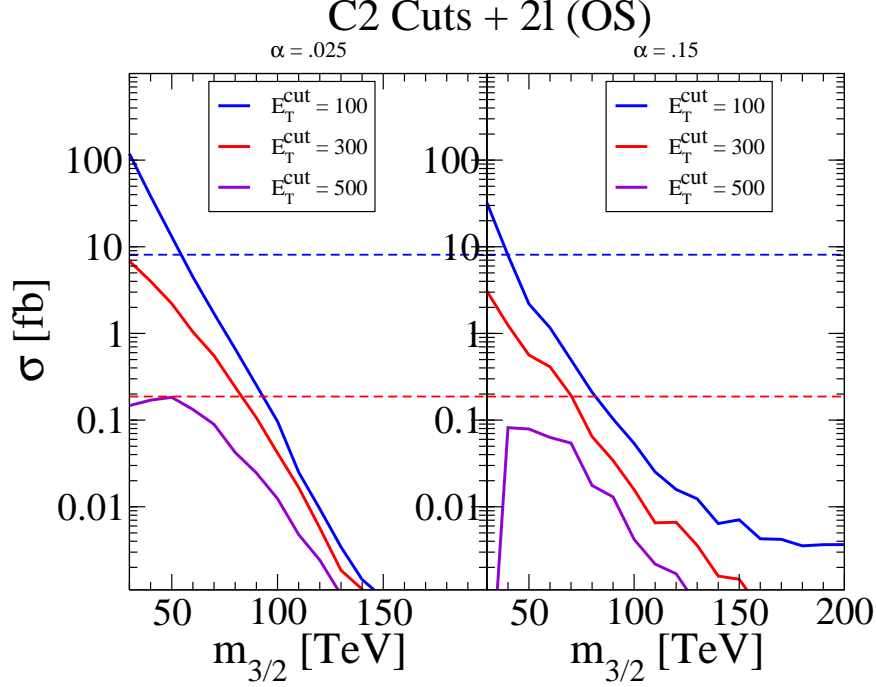


Figure 23: Cross section for multi-jet plus E_T^{miss} events with $n(\ell) = 2$ (OS) at the LHC after cuts $C2$ listed in the text with $E_T^c = 100, 300$ and 500 GeV, versus $m_{3/2}$, from HCAMSB model points with $\tan\beta = 10$, $\mu > 0$ and a). $\alpha = 0.025$ and b). $\alpha = 0.15$. We also list the 100 fb^{-1} 5σ reach with the horizontal lines.

E_T^c (GeV)	0ℓ	1ℓ	OS	SS	3ℓ
100	65/60	65/65	55/40	70/65	80/45
300	105/100	110/105	85/70	-/-	-/-
500	115/105	-/-	-/-	-/-	-/-

Table 3: Estimated reach of 100 fb^{-1} LHC for $m_{3/2}$ (TeV) in two HCAMSB model lines: $\alpha = 0.025$ (upper entry) and $\alpha = 0.15$ (lower entry), in various signal channels.

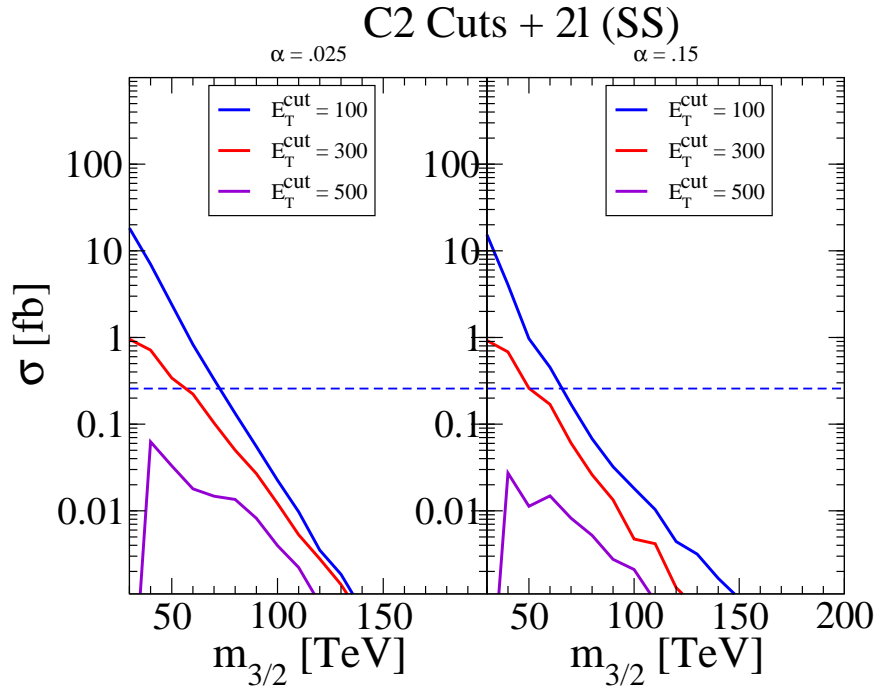


Figure 24: Cross section for multi-jet plus E_T^{miss} events with $n(\ell) = 2$ (SS) at the LHC after cuts $C2$ listed in the text with $E_T^c = 100, 300$ and 500 GeV, versus $m_{3/2}$, from HCAMSB model points with $\tan\beta = 10$, $\mu > 0$ and a). $\alpha = 0.025$ and b). $\alpha = 0.15$. We also list the 100 fb^{-1} 5σ reach with the horizontal lines.

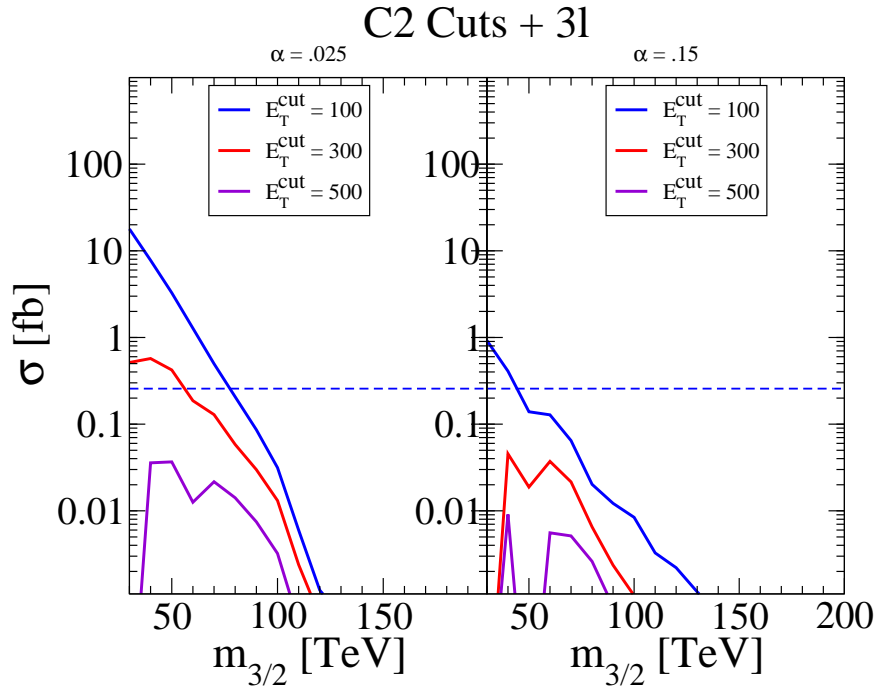


Figure 25: Cross section for multi-jet plus E_T^{miss} events with $n(\ell) = 3$ at the LHC after cuts $C2$ listed in the text with $E_T^c = 100, 300$ and 500 GeV, versus $m_{3/2}$, from HCAMSB model points with $\tan\beta = 10$, $\mu > 0$ and a). $\alpha = 0.025$ and b). $\alpha = 0.15$. We also list the $100 \text{ fb}^{-1} 5\sigma$ reach with the horizontal lines.

tends to be somewhat lower than the reach for mAMSB models, where Ref. [12, 13] finds a 100 fb^{-1} reach of $m_{\tilde{g}} \sim 2.75 \text{ TeV}$ for low values of m_0 . This is due in part because, in mAMSB, the various squark states are more clustered about a common mass scale m_0 , while in HCAMSB the squark states are highly split, with $m_{\tilde{q}_R} \gg m_{\tilde{q}_L} \sim m_{\tilde{g}}$.

The HCAMSB LHC event characteristics suffer similarities and differences with generic mAMSB models. Both HCAMSB and mAMSB give rise to multi-jet plus multi-lepton plus E_T^{miss} event topologies, and within these event classes, it is expected that occasional HITs of length a few cm will be found, arising from production of the long-lived wino-like chargino states. Some of the major differences between the models include the following.

- A severe left-right splitting of scalar masses is expected in HCAMSB, while left-right scalar degeneracy tends to occur in mAMSB. This may be testable if some of the slepton states are accessible to LHC searches. It is well known that in mAMSB, $m_{\tilde{e}_L} \simeq m_{\tilde{e}_R}$, while in HCAMSB, $m_{\tilde{e}_L} \ll m_{\tilde{e}_R}$, since the \tilde{e}_R state has a large weak hypercharge quantum number. In addition, the lightest stau state, $\tilde{\tau}_1$, is expected to be mainly a left- state in HCAMSB, while it is mixed, but mainly a right- state in mAMSB. While it is conceivable that the left-right mixing might be determined at LHC (using branching fractions or tau energy distributions), such measurements would be easily performed at a linear e^+e^- collider, especially using polarized beams[34].
- In HCAMSB models, the light third generation squarks \tilde{t}_1 and \tilde{b}_1 are expected to be generically lighter than the gluino mass, and frequently much lighter. This leads to cascade decays which produce large multiplicities of b and t quarks in the final state. Thus, in HCAMSB models, a rather high multiplicity of b jets is expected. In mAMSB, a much lower multiplicity of b -jets is expected, although this depends also on the value of $\tan\beta$ which is chosen.
- In HCAMSB models, the $U(1)$ gaugino mass M_1 is expected to be the largest of the gaugino masses, with a mass hierarchy of $M_1 > \mu > M_2$. This usually implies that the \tilde{Z}_4 neutralino is mainly bino-like, while \tilde{Z}_2 and \tilde{Z}_3 are higgsino-like, and \tilde{Z}_1 is wino-like. In contrast, in the mAMSB model, usually the ordering is that $\mu > M_1 > M_2$, so that while \tilde{Z}_1 is again wino-like, the \tilde{Z}_2 state is bino-like, and \tilde{Z}_3 and \tilde{Z}_4 are higgsino-like. The compositions of the \tilde{Z}_i for $i > 1$ will not be easy to determine at LHC, but will be more easily determined at a linear e^+e^- collider. However, the mass ordering gives rise to OS dilepton distributions with a prominent $Z \rightarrow \ell^+\ell^-$ peak in HCAMSB, while such a peak should be largely absent in mAMSB models (except at large $\tan\beta$ where there is greater mixing in the neutralino sector). Thus, cascade decay events containing HITs along with a $Z \rightarrow \ell^+\ell^-$ peak in the OS dilepton invariant mass distribution may be a smoking gun signature for HCAMSB models at the LHC, at least within the lower range of $\tan\beta$.

Acknowledgments

This work was supported in part by the U.S. Department of Energy.

References

- [1] L. Randall and R. Sundrum, *Nucl. Phys.* **B 557** (1999) 79; G. Giudice, M. Luty, H. Murayama and R. Rattazzi, *J. High Energy Phys.* **12** (1998) 027.
- [2] I. Jack and D. R. T. Jones, *Phys. Lett.* **B 465** (1999) 148.
- [3] R. Dermisek, H. Verlinde and L-T. Wang, *Phys. Rev. Lett.* **100** (2008) 131804.
- [4] S. Kachru, L. McAllister and R. Sundrum, *J. High Energy Phys.* **0710** (2007) 013.
- [5] H. Verlinde, L-T. Wang, M. Wijnholt and I. Yavin, *J. High Energy Phys.* **0802** (2008) 082; M. Buican, D. Malyshev, D. R. Morrison, H. Verlinde and M. Wijnholt, *J. High Energy Phys.* **0701** (2007) 107.
- [6] P. Langacker, G. Paz, L. T. Wang and I. Yavin, *Phys. Rev. Lett.* **100** (2008) 041802.
- [7] F. Paige, S. Protopopescu, H. Baer and X. Tata, hep-ph/0312045.
- [8] H. E. Haber, R. Hempfling and A. Hoang, *Z. Phys.* **C75** (1997) 539.
- [9] D. Pierce, J. Bagger, K. Matchev and R. Zhang, *Nucl. Phys.* **B 491** (1997) 3.
- [10] G. Belanger, S. Kraml and A. Pukhov, *Phys. Rev.* **D 72** (2005) 015003.
- [11] T. Gherghetta, G. Giudice and J. Wells, *Nucl. Phys.* **B 559** (1999) 27; J. L. Feng, T. Moroi, L. Randall, M. Strassler and S. Su, *Phys. Rev. Lett.* **83** (1999) 1731; J. L. Feng and T. Moroi, *Phys. Rev.* **D 61** (2000) 095004; F. Paige and J. Wells, hep-ph/0001249; A. Datta and K. Huitu, *Phys. Rev.* **D 67** (2003) 115006; S. Asai, T. Moroi, K. Nishihara and T. T. Yanagida, *Phys. Lett.* **B 653** (2007) 81; S. Asai, T. Moroi and T. T. Yanagida, *Phys. Lett.* **B 664** (2008) 185.
- [12] H. Baer, J. K. Mizukoshi and X. Tata, *Phys. Lett.* **B 488** (2000) 367.
- [13] A. J. Barr, C. Lester, M. Parker, B. Allanach and P. Richardson, *J. High Energy Phys.* **0303** (2003) 045.
- [14] See H. Baer and X. Tata, *Weak Scale Supersymmetry: From Superfields to Scattering Events*, (Cambridge University Press, 2006)
- [15] H. C. Cheng, B. Dobrescu and K. Matchev, *Nucl. Phys.* **B 543** (1999) 47.
- [16] R. Dermisek and H. D. Kim, *Phys. Rev. Lett.* **96** (2006) 211803.
- [17] R. Dermisek, *Mod. Phys. Lett.* **A 24** (2009) 1631.
- [18] LEPSUSYWG, note LEPSUSYWG/02-04.1.
- [19] H. Baer, C. H. Chen, F. Paige and X. Tata, *Phys. Rev.* **D 49** (1994) 3283.
- [20] H. Baer and M. Brhlik, *Phys. Rev.* **D 55** (1997) 3201; H. Baer, M. Brhlik, D. Castano and X. Tata, *Phys. Rev.* **D 58** (1998) 015007.
- [21] M. Misiak *et al.*, *Phys. Rev. Lett.* **98** (2007) 022002.

- [22] E. Barberio *et al.* (Heavy Flavor Averaging Group), hep-ex/0603003.
- [23] H. Baer, C. Balazs, J. Ferrandis and X. Tata, *Phys. Rev. D* **64** (2001) 035004.
- [24] T. Moroi and L. Randall, *Nucl. Phys. B* **570** (2000) 455.
- [25] L. F. Abbott and P. Sikivie, *Phys. Lett. B* **120** (1983) 133; J. Preskill, M. Wise and F. Wilczek, *Phys. Lett. B* **120** (1983) 127; M. Dine and W. Fischler, *Phys. Lett. B* **120** (1983) 137; M. Turner, *Phys. Rev. D* **33** (1986) 889.
- [26] K. Rajagopal, M. Turner and F. Wilczek, *Nucl. Phys. B* **358** (1991) 447; L. Covi, J. E. Kim and L. Roszkowski, *Phys. Rev. Lett.* **82** (1999) 4180; L. Covi, H. B. Kim, J. E. Kim and L. Roszkowski, *J. High Energy Phys.* **0105** (2001) 033; for recent reviews, see L. Covi and J. E. Kim, arXiv:0902.0769 and F. Steffen, *Eur. Phys. J. C* **59** (2009) 557.
- [27] H. Baer, A. Box and H. Summy, *J. High Energy Phys.* **0908** (2009) 080.
- [28] Prospino, by W. Beenakker, R. Hopker and M. Spira, arXiv:hep-ph/9611232.
- [29] H. Baer, V. Barger, A. Lessa and X. Tata, arXiv:0907.1922 (2009).
- [30] R. Kadala, J. K. Mizukoshi and X. Tata, *Eur. Phys. J. C* **56** (2008) 511.
- [31] H. Baer, V. Barger, G. Shaughnessy, H. Summy and L. T. Wang, *Phys. Rev. D* **75** (2007) 095010.
- [32] H. Baer, H. Prosper and H. Summy, *Phys. Rev. D* **77** (2008) 055017; H. Baer, A. Lessa and H. Summy, *Phys. Lett. B* **674** (2009) 49.
- [33] H. Baer, C. H. Chen, F. Paige and X. Tata, *Phys. Rev. D* **52** (1995) 2746 and *Phys. Rev. D* **53** (1996) 6241; H. Baer, A. Belyaev, T. Krupovnickas and X. Tata, *Phys. Rev. D* **65** (2002) 075024.
- [34] H. Baer, R. Munroe and X. Tata, *Phys. Rev. D* **54** (1996) 6735.